Journal of Materials Chemistry B

ROYAL SOCIETY OF CHEMISTRY

PAPER

View Article Online
View Journal | View Issue

Cite this: J. Mater. Chem. B, 2026, 14, 3743

Incorporation of NU-1000 into cellulose acetate membranes with preserved indoxyl sulfate adsorption

Rita F. Pires, [a] Beatriz S. Nunes, [a] Flávia S. C. Rodrigues, *[a] Anup Paul, [b] Ana Charas, [c] Anirban Kamakar [d] and Mónica Faria [ae]

Zirconium-based metal–organic framework (MOF) NU-1000 was successfully synthesized and exhibited the expected structural and chemical properties, confirming its suitability as an adsorbent for protein-bound uremic toxins (PBUTs). In batch experiments, NU-1000 removed approximately 53% of indoxyl sulfate (IS), corresponding to an adsorption capacity of 17.7 mg IS g^{-1} NU-1000. To translate this adsorption capability into a membrane platform, mixed matrix membranes (MMMs) were prepared by incorporating NU-1000 into a cellulose acetate (CA) matrix *via* phase inversion. Structural characterization confirmed the uniform dispersion of NU-1000 microcrystals within the polymer, with no evidence of agglomeration or degradation during fabrication. The resulting membranes exhibited an asymmetric morphology, consisting of a dense selective layer supported by a porous substructure, while maintaining good hydrophilicity (contact angle $<60^{\circ}$) and structural integrity. Under crossflow filtration of buffered IS solutions, CA/NU-1000 membranes showed a 1.3-fold increase in IS transport compared to pristine CA membranes. This enhancement indicates that NU-1000 retains its adsorption functionality after incorporation into the polymer matrix and contributes to adsorption-assisted transport. The reversible interactions between IS and NU-1000 enhance solute partitioning within the membrane, promoting diffusion and increasing permeation. Overall, these results demonstrate that CA/NU-1000 MMMs combine the processability and transport properties of conventional polymeric membranes with MOF-based adsorption, offering a promising strategy for adsorption-assisted transport and improved clearance of PBUTs in hemodialysis.

Received 1st January 2026,
Accepted 27th February 2026

DOI: 10.1039/d6tb00006a

rsc.li/materials-b

1. Introduction

Chronic kidney disease (CKD) is a progressive disorder characterized by the gradual loss of kidney function over time. In advanced stages, CKD can progress to end-stage renal disease (ESRD), at which point renal replacement therapies such as hemodialysis (HD) or kidney transplantation become necessary.[1] During HD, water and small solutes are removed, but remains an incomplete detoxification process, as it cannot eliminate all of the more than 140 uremic toxins (UTs) identified to date, particularly protein-bound uremic toxins (PBUTs). These include low-molecular-weight compounds such as indoxyl sulfate (IS) and *p*-cresyl sulfate (pCS), which bind tightly to plasma proteins, especially human serum albumin (HSA). Since only the free form, unbound fraction of PBUTs can cross the dialysis membrane, their removal efficiency during HD is significantly reduced. As a result, despite regular treatment, PBUTs accumulate in the blood and contribute to persistent uremic symptoms and complications, which have been strongly associated with the high mortality rate observed in ESRD patients.[1–3]

Advances in HD technology, including high-flux membranes and hemodiafiltration (HDF), have been introduced to improve the clearance of higher-molecular-weight UTs. However, even with these developments, the removal of PBUTs remains a major challenge.[1] To address this issue, researchers have focused on the use of binding competitors to displace protein-UT complexes.[4–7] Activated carbon (AC),[8–10] zeolites,[11–14] carbon nanotubes (CNTs),[15,16] and magnetic nanoparticles (MNPs) have been investigated as adsorptive fillers for HD membranes,[17,18] but all of these approaches present limitations for clinical use, mainly

[a] Laboratory of Physics for Materials and Emerging Technologies (LaPMET), Center of Physics and Engineering of Advanced Materials (CeFEMA), Instituto Superior Técnico, Universidade de Lisboa, Lisboa, Portugal. E-mail: flavia.rodrigues@tecnico.ulisboa.pt
[b] VALORIZA, Politécnico de Portalegre, Portalegre, Portugal
[c] Instituto de Telecomunicações, Instituto Superior Técnico, Lisboa, Portugal
[d] Centro de Estudos de Engenharia Química, Instituto Superior de Engenharia de Lisboa, Instituto Politécnico de Lisboa, Lisboa, Portugal
[e] Departamento de Engenharia Química (DEQ), Instituto Superior Técnico, Universidade de Lisboa, Lisboa, Portugal

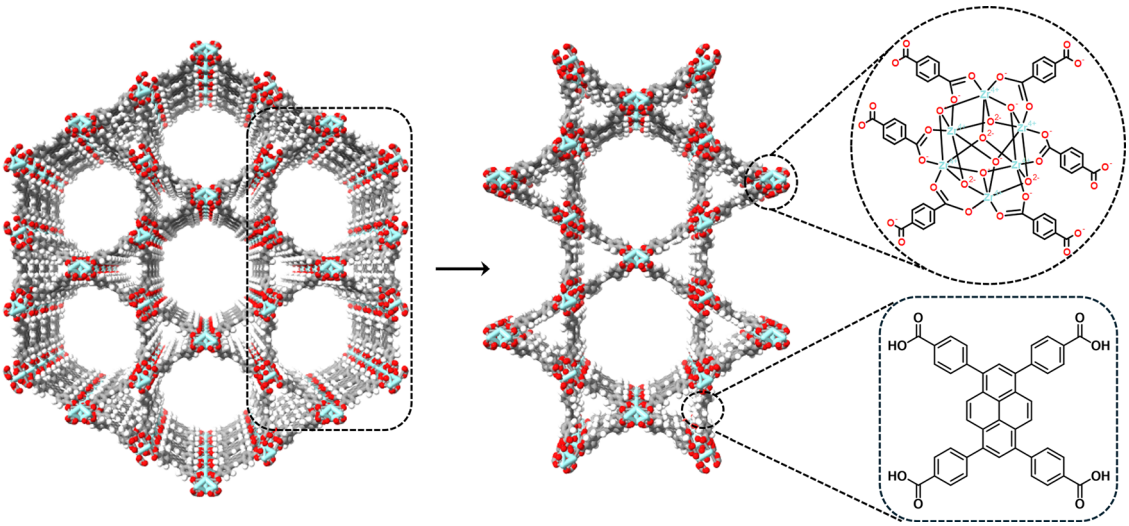

Fig. 1 Schematic illustration of the structure of NU-1000.

due to poor selectivity, fouling and hemocompatibility concerns. These constraints motivate the search for alternative adsorptive materials that can be integrated into HD membranes while ensuring blood compatibility.

Metal–organic frameworks (MOFs) have recently emerged as promising materials for the removal of PBUTs due to their exceptionally high surface area, tunable porosity, and versatile chemical functionality.[19–21] Several MOFs have been investigated for adsorption of representative PBUTs such as IS and pCS, namely iron- (Fe-) and zirconium- (Zr-) based frameworks.[22,23]

Fe-based MOFs have been widely investigated for PBUT removal, such as MIL-100(Fe), due to their high surface area and good biocompatibility, but their performance is strongly reduced in the presence of serum proteins, which limits their relevance for dialysis applications.[22,24–26]

Zr-based MOFs are particularly valued for their exceptional chemical and thermal stability, and several frameworks have been investigated for PBUT adsorption. UiO-66 is one of the most studied examples, and although its pristine form typically shows modest adsorption, functionalized derivatives with amino moieties (UiO-66-NH_2, UiO-66-NH_3) exhibited improved adsorption of indole-3-acetic acid and hippuric acid.[23] Incorporation of UiO-66-$(COOH)_2$ into polyacrylonitrile nanofibers yielded adsorbents with high uptake, excellent reusability, and promising hemocompatibility.[27,28] Nevertheless, the adsorption capacities of UiO-66-based materials remain lower than those reported for NU-1000, particularly for anionic PBUTs such as IS and pCS. These results demonstrate the potential of Zr-based MOFs when combined with polymer supports, although concerns about zirconium toxicity and scalability remain important barriers to clinical translation.

Within the family of Zr-based MOFs, NU-1000 has emerged as one of the most promising candidates for PBUT removal due to its large accessible channels, strong affinity for anionic toxins, and excellent aqueous stability. NU-1000 is a pyrene-based framework composed of octahedral Zr_6 clusters connected by tetratopic organic linkers, forming a hierarchical porous structure, with large, accessible channels.[29] Fig. 1 depicts this architecture, which combines mesoporous 31 Å hexagonal channels with microporous 12 Å triangular channels, interconnected by orthogonal 10 × 8 Å windows.[24,30,31]

NU-1000 exhibits exceptional chemical and thermal stability, and its high surface area and porosity have contributed to remarkable adsorption capacities under physiological conditions.[32] These properties make NU-1000 one of the most effective Zr-based MOFs for PBUT elimination.

However, despite its superior performance, practical implementation in HD devices is challenged by the dense particle packing of NU-1000 powders and limitations in HD,[24,33,34] highlighting the need for further engineering of its form and surface properties. One promising strategy is to integrate NU-1000 into hemocompatible polymeric matrices, such as cellulose acetate (CA) membranes, thereby combining its high adsorption capacity with the blood compatibility, flexibility, and processability of established dialysis materials. This approach not only addresses the challenges of particle packing and hemocompatibility but also aligns with scalable membrane fabrication techniques, paving the way for practical clinical translation.

Although NU-1000 shows strong intrinsic affinity toward PBUTs, its performance can be substantially influenced by how it is incorporated into a polymeric matrix. Factors such as particle agglomeration, partial coverage by CA, pore obstruction or non-homogeneous distribution may limit the accessible surface area of the MOF and reduce its adsorption capability. For this reason, beyond evaluating PBUT removal, it is essential to understand how NU-1000 is positioned within the CA membrane and whether it remains structurally preserved and accessible under conditions relevant to dialysis. Despite its promising properties, the integration of NU-1000 into dialysis-relevant polymeric membranes and its evaluation under dynamic crossflow conditions have not yet been reported.

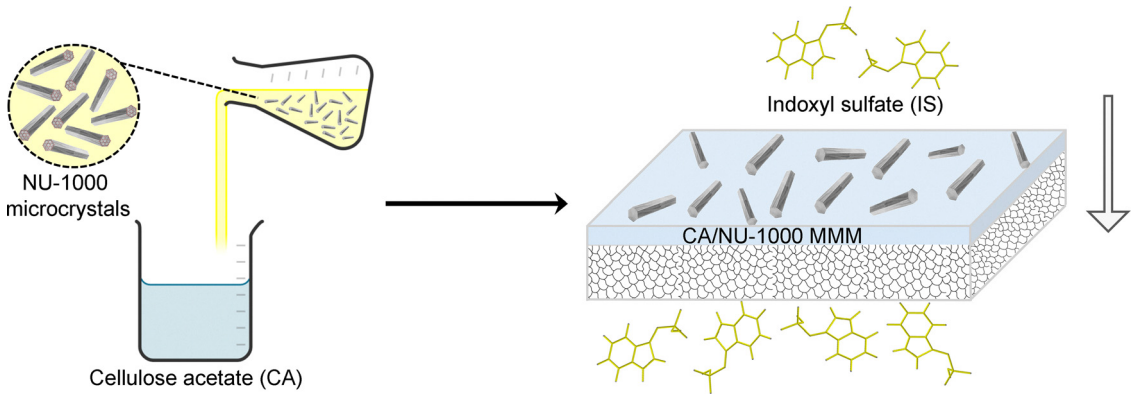

Fig. 2 Schematic representation of CA/NU-1000 mixed matrix membranes (MMMs) fabrication and the crossflow permeation of indoxyl sulfate (IS) through the membrane.

In this work, NU-1000 was incorporated into CA membranes to overcome these limitations, stabilizing the MOF and enhance PBUT removal. Since CA is a low-cost, biodegradable polymer with good hemocompatibility and film-forming properties, offering an eco-friendlier alternative to conventional synthetic dialysis membranes, embedding NU-1000 into CA enables the fabrication of mixed matrix membranes (MMMs) that combine high toxin adsorption with stability and permeability. Their performance was evaluated in phosphate-buffered saline (PBS) with IS, focusing on stability, adsorption, and clearance. Therefore, this study establishes CA/NU-1000 MMMs as a sustainable and efficient strategy to enhance PBUT removal in the context of HD. Fig. 2 schematically summarizes the preparation of CA/NU-1000 MMMs and the permeation assays carried out with buffered IS solution, illustrating IS transport through the membrane under crossflow conditions.

2. Results and discussion

2.1. Synthesis and characterization of NU-1000 MOFs

Fig. 3a shows the attenuated total reflectance-Fourier-transform infrared spectroscopy (ATR-FTIR) spectrum obtained for the H_4TBAPy ligand and the NU-1000 MOF. The vibrational modes at 1600 and 1400 cm^{-1}, which are characteristic of carboxylate stretches, are assigned to the asymmetric and symmetric stretching vibrations of coordinated carboxylate (COO^-) groups, respectively.[35,36] The calculated separation ($\Delta\nu \approx 200$ cm^{-1}) falls within the typical range reported for bridging/bidentate coordination of carboxylates to Zr_6 oxo-clusters in Zr-based MOFs, confirming successful deprotonation of H_4TBAPy and its coordination to the Zr nodes within the NU-1000 framework. No bands near 1700–1720 cm^{-1} (free –COOH) and 1660–1670 cm^{-1} (residual DMF) were observed,[35,36] further supporting effective linker coordination and solvent removal after activation. Additionally, the distinct peaks at 780, 710, and 650 cm^{-1} are attributed to the longitudinal and transverse vibrational modes of the Zr–O bonds, which are consistent with Zr–O and Zr–O–C vibrations associated with the Zr_6O_8 clusters of NU-1000.[37,38] Thermogravimetric analysis (TGA) was carried out to evaluate the thermal stability and to obtain the optimal activation temperature for the NU-1000 MOF. Fig. 3b reveals two prominent thermal events denoted as zone 1, between 40 and 400 °C, and zone 2, between 400 and 580 °C. The initial 28% mass loss is indicative of the removal of entrapped impurities such as solvent (DMF), water, and potential hydroxyl groups. The more pronounced mass loss (55%) observed in zone 2 is attributed to the onset of thermal decomposition of the framework.[39] This implies that the NU-1000 framework maintains stability up to 400 °C, beyond which degradation of the TBAPy linkers commences.

Fig. 3c shows the diffraction patterns obtained by powder X-ray diffraction (PXRD), where three distinct and well-defined peaks can be identified, with the first two being of greater intensity. Although simulated NU-1000 patterns display multiple reflections, only three distinct and well-defined peaks are prominently observed experimentally. This may be attributed to preferred orientation effects of the hexagonal rod-like crystals and the reduced intensity of higher-angle reflections. The clarity in the peak pattern, together with the similarity of peaks found by Wang *et al.*,[35] suggests a high degree of crystallinity of the sample. The nitrogen adsorption isotherm of the NU-1000 MOF shown in Fig. 3d is of Type I, which is indicative of microporous adsorbents. Results show that the Brunauer–Emmett–Teller (BET) surface area of the MOF was 2256 m^2 g^{-1}, the pore volume 1.39 cm^3 g^{-1}, and the pore diameter 25.34 Å. These values are comparable to previously reported values of 2200 m^2 g^{-1},[31] 1.37 cm^3 g^{-1},[31] and 27.3–31.0 Å,[32,35] indicating that the synthesized material preserves the characteristic porosity of NU-1000.

The scanning electron microscopy (SEM) micrographs of NU-1000 microparticles (Fig. 3e) display the characteristic hexagonal rod-like morphology typical of this MOF. Each crystal is composed of six smooth rectangular facets that assemble into well-defined hexagonal cylinders, with average lengths of 2.5 ± 0.8 μm (measured using ImageJ 2.3.0, 3000× magnification, n = 20). These dimensions are consistent with previously reported values, where NU-1000 crystal sizes typically range between 1.5 and 10 μm.[40,41] The energy-dispersive X-ray spectroscopy (EDS) spectrum (Fig. 3f) shows 46.7 wt% C, 15.8 wt% O and 20.1 wt% Zr. These results indicate that the NU-1000 MOFs are composed of the metallic Zr nodes and the organic H_4TBAPy ligand. The Au signal (17.5 wt%) is associated

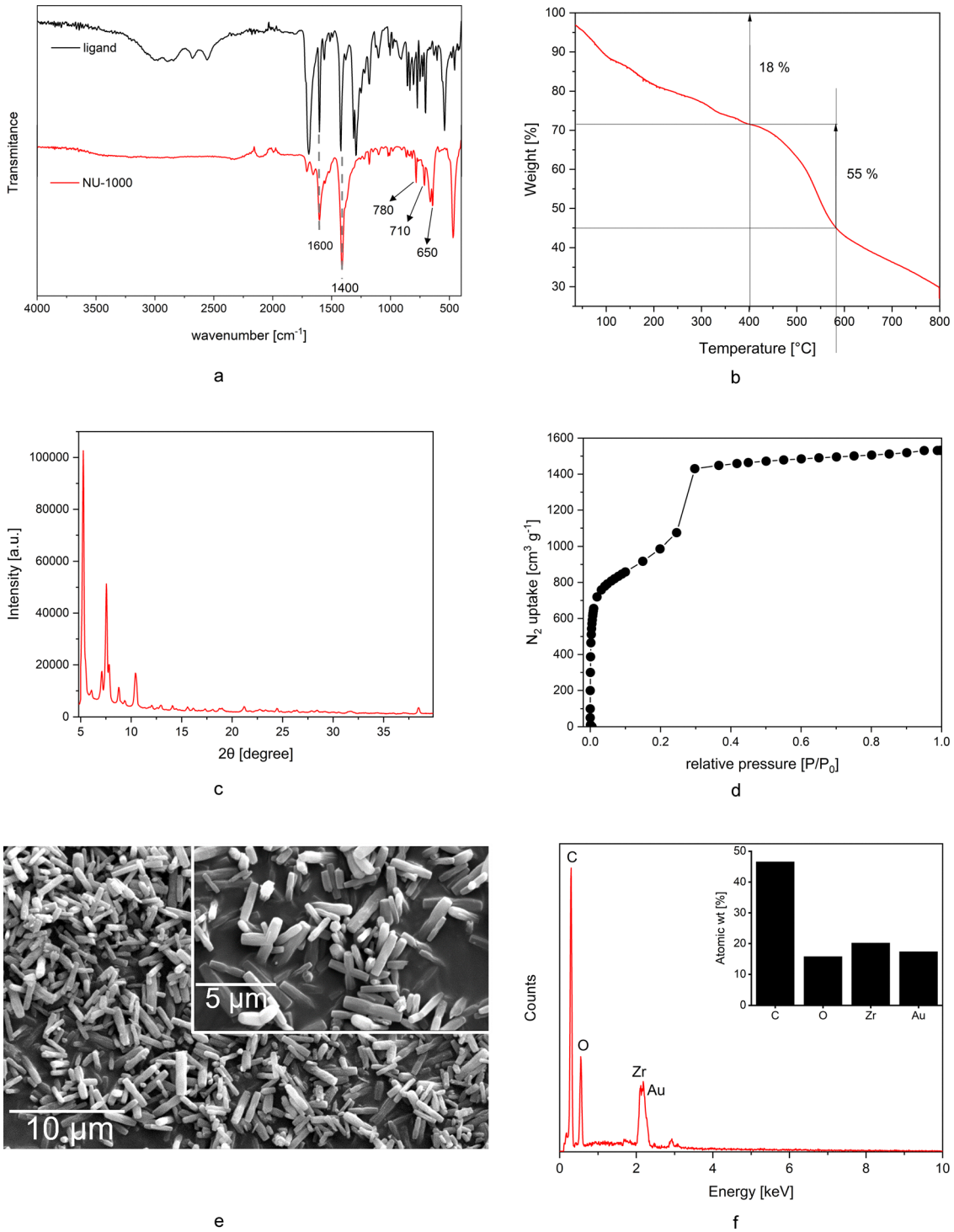

Fig. 3 Characterization of NU-1000 MOFs: (a) ATR-FTIR spectra of the H_4TBAPy ligand and NU-1000 MOF; (b) TGA curve; (c) PXRD patterns; (d) nitrogen adsorption isotherm; (e) SEM images of NU-1000 particles at 3000× and 7000× magnification (inset); and (f) EDS spectra and atomic weight percentage of each element (inset).

with the sputter-coating applied prior to SEM analysis and is not related to the MOF structure.

Overall, the synthetized NU-1000 MOF exhibits the crystallinity, morphology, thermal stability and porosity characteristics of this MOF, which confirms its suitability for subsequent incorporation into CA membranes.

2.2. Adsorption of indoxyl sulfate by NU-1000 MOFs in phosphate-buffered saline

Fig. 4a shows the evolution of IS concentration in PBS over a 180-minute period, comparing solutions with NU-1000 (grey bars) to the negative control without MOFs (white bars). In the control,

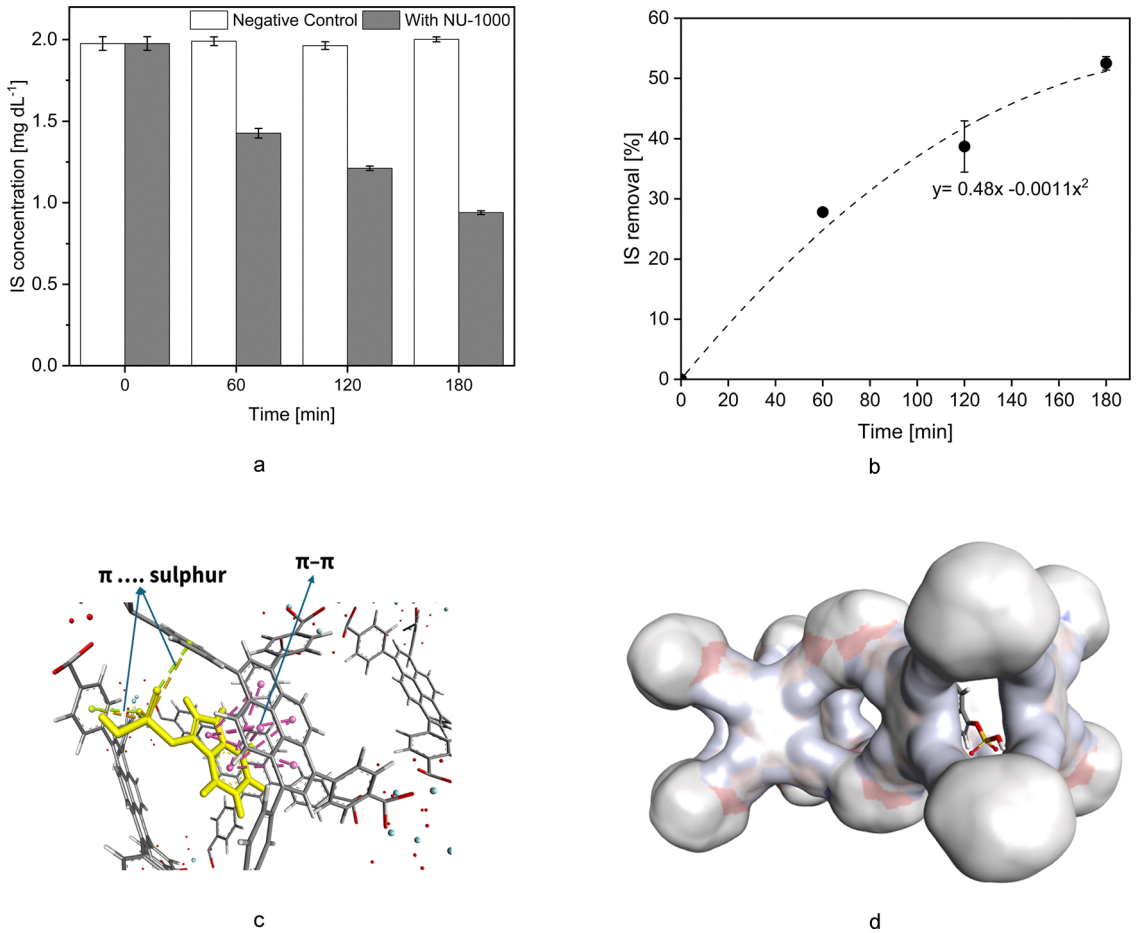

Fig. 4 (a) Indoxyl sulfate (IS) concentration in PBS solutions over time, with (grey) and without (white) NU-1000 MOFs; (b) IS removal efficiency (%) by 6 mg NU-1000 MOFs from a 2.0 mg dL^{-1} IS solution in PBS, as a function of time; (c) non-covalent interactions between NU-1000 and IS (color codes: IS: yellow); (d) surface filed view of the docking of IS with NU-1000.

IS concentration remained stable at ~2.0 mg dL^{-1}, confirming no degradation or loss of IS in the absence of adsorbent. In contrast, the presence of 6 mg of NU-1000 led to a steady decline in IS concentration, reaching 0.94 ± 0.01 mg dL^{-1} after 180 minutes. This corresponds to ~53% removal of the initial IS (Fig. 4b; 17.7 mg IS g^{-1} NU-1000), demonstrating the strong adsorption capacity of NU-1000.

These findings are consistent with those reported in the literature obtained under similar ionic strength conditions. Zhang *et al.*,[30] reported an adsorption capacity of 18.9 mg IS g^{-1} for ZJU-X6 in saline media, which is comparable to the value obtained in this work (17.7 mg IS g^{-1} NU-1000). In the same study, a significantly higher capacity was observed in pure water (35 mg IS g^{-1} ZJU-X6), indicating a marked reduction in adsorption performance in the presence of salts. This trend highlights the strong influence of ionic strength on MOF–IS interactions, likely due to charge screening and competition effects.

When compared with other adsorbents evaluated under buffered conditions, the performance of NU-1000 is within the range reported for state-of-the-art materials. Polymeric adsorbents such as H-PES/SPSf@PEI microspheres exhibit lower adsorption capacities (~5.5 mg IS g^{-1} H-PES/SPSf@PEI),[42] whereas nitrogen-containing porous carbon adsorbents (NPCA) can reach higher values (~30.5 mg IS g^{-1} NPCA).[43] These comparisons place NU-1000 among competitive adsorbents under physiologically relevant conditions.

For completeness, adsorption studies performed in pure water generally report higher removal efficiencies. For example, Kato *et al.*[32] observed ~92% IS removal within 1 minute using NU-1000 in a 0.1 mM IS solution prepared in pure water (pH 6.5). However, no evaluation was conducted under buffered or saline conditions, limiting direct comparison with the present work. The slower adsorption kinetics and lower apparent capacity observed here are therefore attributed to the use of PBS, where increased ionic strength reduces electrostatic interactions between IS and the MOF surface, in agreement with previous observations for saline systems.

To understand the mechanisms underlying IS adsorption, molecular docking studies were performed.[44,45] The results indicate that IS binds favorably within the NU-1000 framework through multiple non-covalent interactions. The sulfate moiety of IS forms hydrogen bonds with the hydroxyl groups and metal-oxo clusters of NU-1000, while the indole ring engages in π–π stacking with the aromatic linkers (Fig. 4c). These interactions are further

reinforced by electrostatic attractions, collectively stabilizing the IS-NU-1000 complex. The pore architecture of NU-1000 provides a well-defined binding pocket with complementary charge distribution, ensuring efficient accommodation of IS and explaining the high adsorption capacity observed experimentally (Fig. 4c and d).

The theoretical insights are consistent with experimental findings. The predicted hydrogen bonding, π–π stacking, and electrostatic interactions not only rationalize the steady decrease in IS concentration over time but also account for the stable retention of IS within the framework.

Together, the experimental and computational results highlight NU-1000's effectiveness as an adsorbent, demonstrating how its high porosity, Zr-based nodes, and tailored pore environment synergistically promote strong host–guest interactions. These results demonstrate the intrinsic adsorption performance of NU-1000 prior to its incorporation into a polymeric matrix, thus providing a reference point for evaluating whether the MOF retains its function once embedded in CA membranes. The synergy between theory and experiment not only validates the adsorption behavior of NU-1000 but also establishes a foundation for the rational design of MOF-based platforms for the removal of PBUTs and other clinically relevant molecules.

2.3. Fabrication and characterization of CA and CA/NU-1000 membranes

The pure CA membranes and NU-1000-containing MMMs exhibited similar visual properties. Fig. 5 shows representative photographs of the CA-10 membrane and the CA/NU-1000-10 MMM. Pure CA membranes appeared white (Fig. 5a), whereas MMMs displayed a light-yellow tint (Fig. 4b), attributed to the bright yellow color of NU-1000. Despite containing 2 wt% of solid MOF, the MMMs maintained high flexibility and showed no signs of brittleness, similar to the pure CA membranes.

2.3.1. Membrane morphology by scanning electron microscopy. Fig. 6 shows the SEM images of the active layers, porous surfaces, and cross sections of the CA-0, CA/NU-1000-0, CA-10 and CA/NU-1000-10 membranes.

The active layer of all membranes appears dense and free of visible pores, which is typical of integral asymmetric membranes produced by the phase inversion method.[46] In contrast, the porous surfaces display non-uniform structures with occasional visible pores, indicative of the underlying support layer. This support layer contributes to the mechanical strength of the membrane while enabling solute transport across the membrane with minimal resistance.

Cross-sectional SEM micrographs reveal the asymmetric structure of the membranes, consisting of a very thin dense skin layer at the top and a much thicker and more porous sublayer beneath. The measured total thicknesses were 115 ± 1.0 μm, 92 ± 0.4 μm, 95 ± 0.2 μm, and 91 ± 0.6 μm for the CA-0, CA/NU-1000-0, CA-10, and CA/NU-1000-10 membranes, respectively. These results indicate that MMMs incorporating NU-1000 are thinner than their corresponding pure CA counterparts.

NU-1000 microparticles are clearly visible on the active layer surfaces of CA/NU-1000-0 and CA/NU-1000-10, appearing as elongated, cylindrical particles consistent with the rod-like morphology observed on the crystals in powder form. Quantitative analysis of three distinct regions per membrane at 3000× magnification using ImageJ revealed that NU-1000 occupied average surface areas of 4.4 ± 0.6% and 4.2 ± 0.7% for the CA/NU-1000-0 and CA/NU-1000-10 membranes, respectively. The relatively low surface coverage was expected, given the much lower proportion of NU-1000 in the casting solutions compared to CA polymer (2.3 wt% compared to 97.7 wt%).

2.3.2. Surface chemistry by energy-dispersive X-ray spectroscopy and chemical composition by attenuated total reflection – Fourier transform infrared spectroscopy. Fig. 7a and b show the EDS spectra obtained from different regions (3000× amplification) of the CA/NU-1000-0 and CA/NU-1000-10 MMMs, respectively. When the analysis was performed in regions where NU-1000 MOFs are clearly visible, zirconium (Zr) was detected, with atomic weight percentages (wt%) of 13 and 12 for CA/NU-1000-0 and CA/NU-1000-10, respectively. Other elements detected in these regions included carbon (53–57 wt%) and oxygen (17–22 wt%). In contrast, spectra regions where MOFs were not visible do not show a Zr peak. In these regions, only carbon (61–68 wt%) and oxygen (17–20 wt%), which are the main elements of CA, were detected. The presence of carbon and oxygen in MOF-containing regions can be attributed either to the organic linker of NU-1000 or to a thin CA layer partially covering the MOFs.

Fig. 7c shows the ATR-FTIR spectra of the CA-10 and CA/NU-1000-10 membranes. As reported in previous studies,[47–49] the characteristic bands of CA are clearly identified. The broad band centered at 3478 cm^{-1} corresponds to the OH stretching

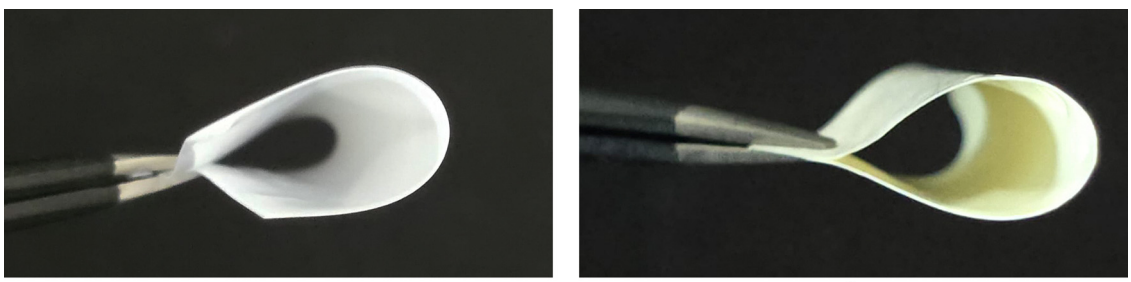

Fig. 5 Photographs of (a) pure CA-10 membrane, and (b) CA/NU-1000-10 mixed matrix membrane (MMM) (2 wt% NU-1000).

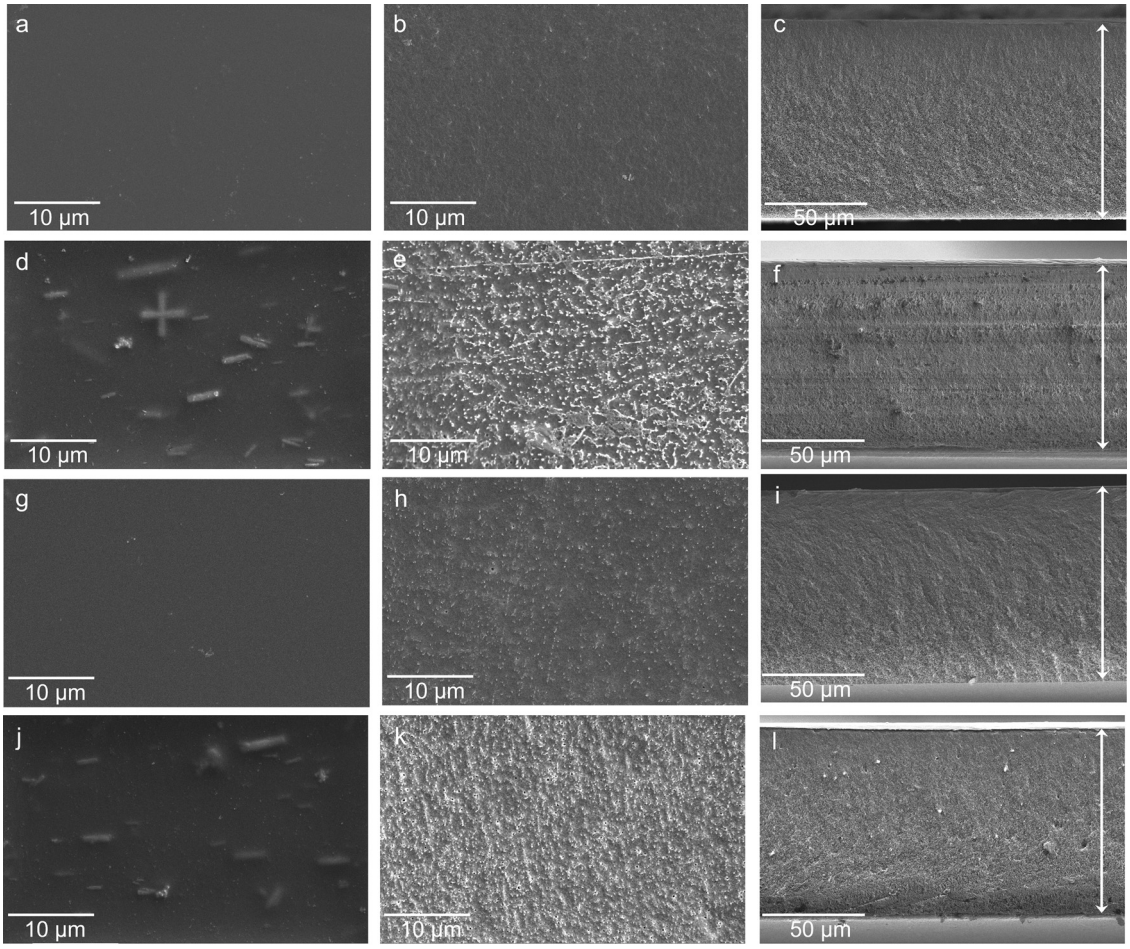

Fig. 6 SEM images of the membranes: CA-0 (a–c), CA/NU-1000-0 (d–f), CA-10 (g–i) and CA/NU-1000-10 (j–l). Active layers (left column – a, d, g and j; 3000× magnification), porous surfaces (middle column – b, e, h and k; 3000× magnification) and cross sections (right column – c, f, i and l; 700× magnification).

vibration, ν(OH), of non-esterified cellulose hydroxyl groups. The strong peak at 1747 cm^{-1} is assigned to the carbonyl stretching vibration, ν(C═O). The band at 1380 cm^{-1} is attributed to CH deformation, $\delta(CH_3)$. Stronger peaks at 1234 cm^{-1} and 1051 cm^{-1} correspond to C–O stretching modes.

In the CA/NU-1000-10 membrane, in addition to the peaks which are characteristic of CA, new absorption bands appear. A broad band at 2918 cm^{-1} is attributed to the C–H stretching vibration, ν(CH), of the aromatic organic linker. Peaks at 1543 and 1431 cm^{-1} are assigned to the asymmetric and symmetric stretching vibrations of the carboxylate groups of the linker. Finally, the peak at 769 cm^{-1} corresponds to Zr–O longitudinal vibrations, confirming the presence of NU-1000 in the membrane. EDS and ATR-FTIR analyses confirm the presence of NU-1000 within the CA matrix, indicating that the MOF retains its chemical characteristics after membrane fabrication.

2.3.3. Internal structure of CA/NU-1000-10 by 3D X-ray microscopy. Fig. 8a shows the reconstructed 3D model of the CA/NU-1000-10 membrane with the active dense layer facing upward. High-density regions are represented in lime, whereas lower-density areas appear in black or darker shades. The active layer is composed of a dense CA polymer matrix. Large yellow particles visible on the surface are dirt or foreign materials and were excluded from the analysis.

To focus on the internal structure and avoid misleading calculations, the outer surfaces were removed (Fig. 8b). By assigning different densities to CA and NU-1000, NU-1000 microparticles were isolated and visualized in orange (Fig, 8c). NU-1000 was found to be homogeneously distributed throughout the membrane, occupying 0.59% (2.8×10^{-4} mm^3) of the analyzed internal volume (0.05 mm^3). The length of NU-1000 MOFs ranged from 0.5 to 7.8 μm, with ~42% falling between 1.8 and 3.0 μm (Fig. 8d). This uniform distribution and the preserved particle size range suggests that the membrane fabrication process does not promote significant NU-1000 aggregation or apparent structural degradation within the CA matrix.

Fig. 8e shows the spatial distribution of voids, with colors indicating diameter: black (~0 μm), dark blue (~3 μm), and light blue (~6 μm). The active layer is dense with almost no voids, while the support layer exhibits increasing void diameter from top to bottom, with light blue and occasional pink regions

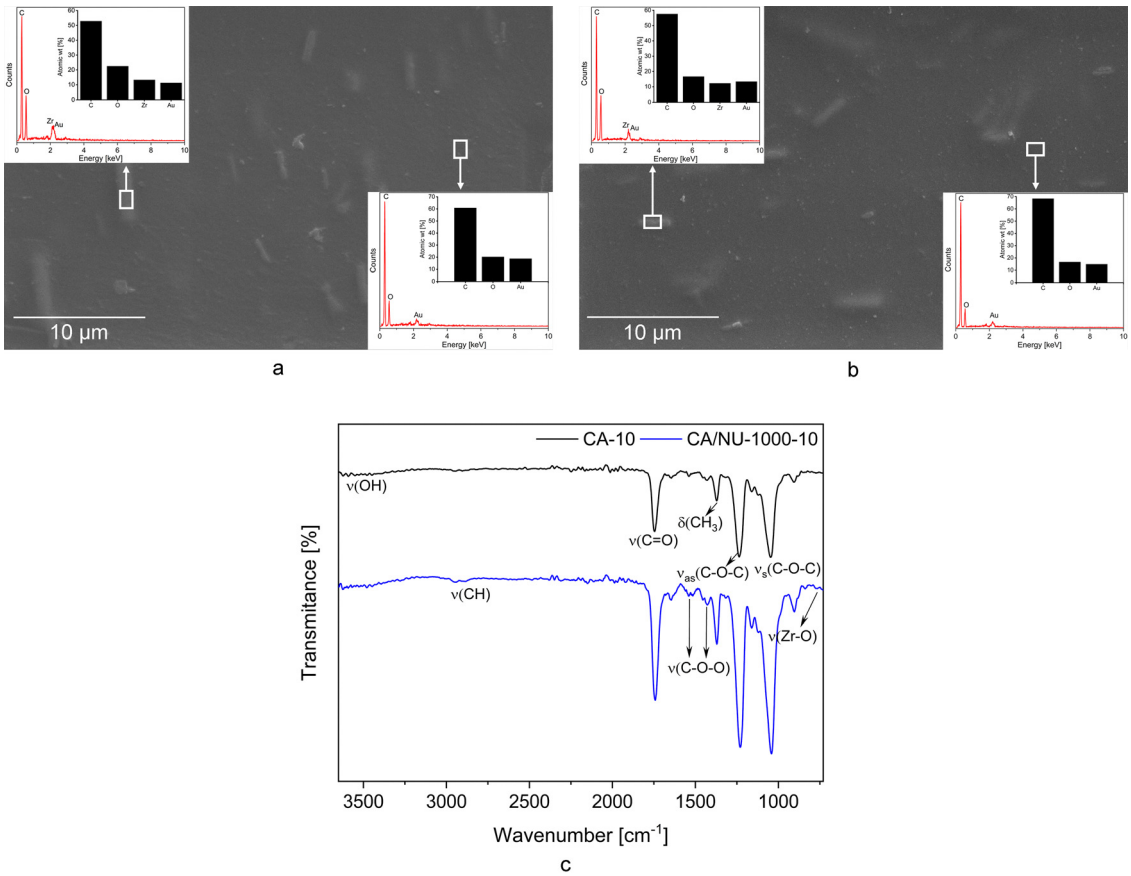

Fig. 7 SEM images of (a) CA/NU-1000-0, and (b) CA/NU-1000-10 (3000× magnification) and EDS spectra and atomic weight percentage of elements present in two different regions of the membrane (inset); (c) ATR-FTIR spectra of the CA-10 (black) and CA/NU-1000-10 (blue) membranes.

at the base. Quantitative analysis (Fig. 8f) revealed that voids occupy 60% of the membrane volume, with a predominance (41%) of voids between 4.2 and 5.4 μm in diameter.

CT-scan analysis determined a modal membrane thickness between 90 and 104 μm, observed in approximately 80% of the analyzed cross-sections. These values are in good agreement with the thickness obtained from SEM cross-sectional analysis (Section 2.3.1), which reported 91 ± 0.6 μm for CA/NU-1000-10, confirming the consistency between the two characterization techniques.

Three-dimensional tomography reconstruction revealed an asymmetric membrane structure consisting of a thin dense skin layer supported by a thicker porous substructure. This observation is consistent with the SEM cross-sectional analysis (Section 2.3.1), where the active layer was described as dense and free of visible pores. The porous support accounts for approximately 60% of the total membrane volume, indicating a highly open internal structure with low intrinsic resistance to flow. The measured hydraulic permeability (Section 2.3.6) reflects the overall transport properties of the membrane, which are primarily governed by the characteristics of the selective layer. The presence of a dense skin layer is consistent with the measured MWCO values, confirming that membrane selectivity is controlled by this top layer, while the underlying porous structure mainly facilitates transport. In addition, the porous support provides mechanical stability to the thin dense layer, contributing to the overall structural integrity of the membrane.

2.3.4. Surface topography by atomic force microscopy. The active layer surfaces of the dried CA-0, CA/NU-1000-0, CA-10, and CA/NU-1000-10 membranes were analyzed by atomic force microscopy (AFM). Fig. 9 shows the topography and phase AFM images together with height profile plots taken at the indicated positions of the active surface of the CA-0, CA/NU-1000-0 (scan area of 3 μm × 3 μm), CA-10, and CA/NU-1000-10 (scan area of 2 μm × 2 μm) membranes.

The AFM topography image of the CA-0 membrane reveals a surface exhibiting moderately elevated, and almost regularly spaced longitudinal features. Such morphology is typically associated with confined crystallization processes that promote lamellar orientation, which can be affected by factors including temperature, film thickness, and substrate–polymer interactions. This phenomenon is commonly observed in the assembly of multilayered films.[50] A comparable surface morphology to CA-0 was also reported by Faria *et al.*[51] for hybrid flat-sheet CA/silica ultrafiltration (UF) membranes. In their study, CA-based membranes containing 5 wt% SiO_2 exhibited parallel and uniform ridges with an average spacing of 2.5 μm on the top dense

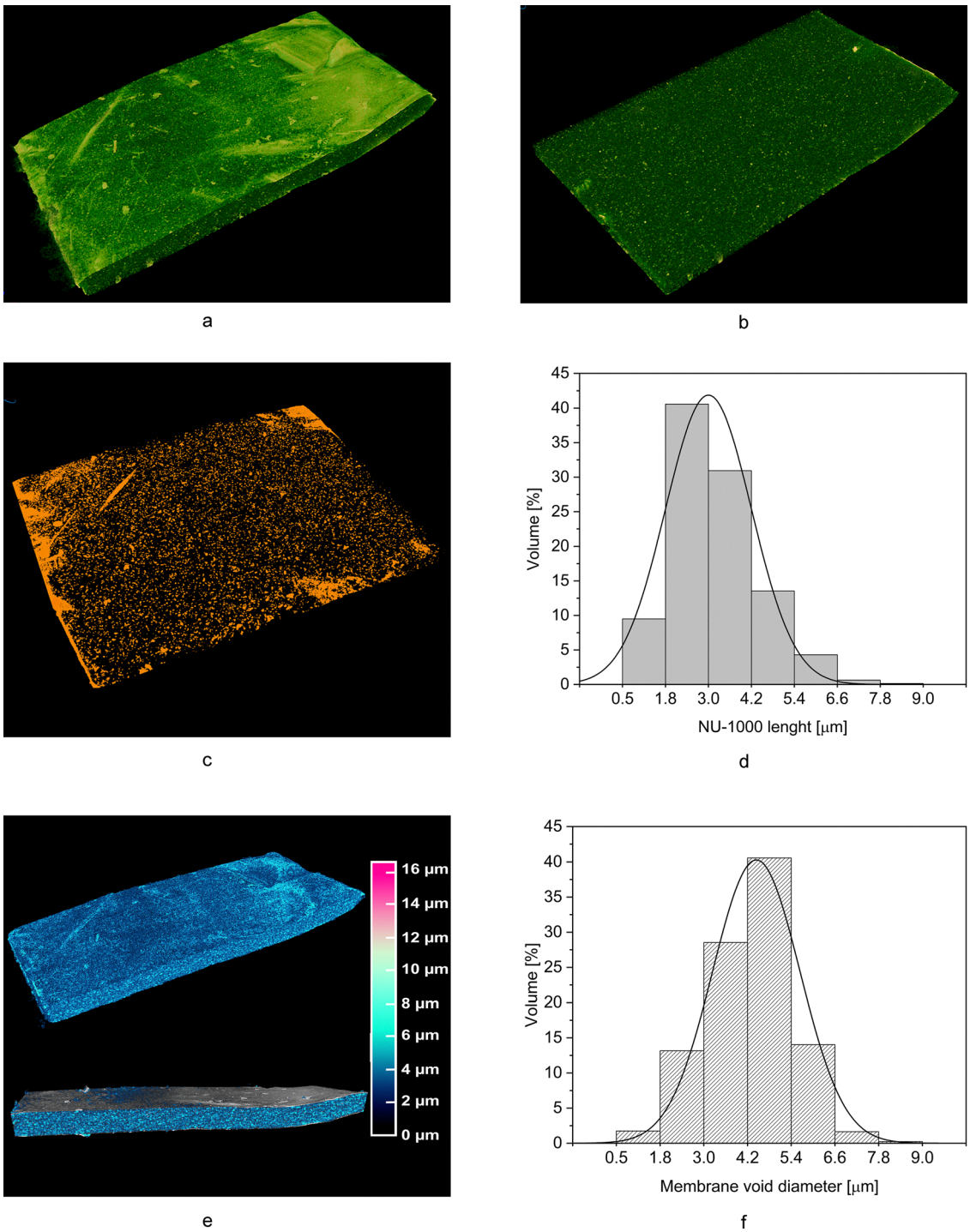

Fig. 8 3D X-ray microscopy analysis of CA/NU-1000-10 membrane: (a) reconstructed 3D model of the entire membrane with the active layer facing upward; (b) internal structure after removing outer surfaces; (c) distribution of NU-1000 microparticles (orange); (d) length distribution of NU-1000 microparticles; (e) reconstructed 3D model of void distribution, with colors indicating void diameter from black (~0 μm) to dark blue (~3 μm) to light blue (~6 μm); (f) distribution of void diameters.

surface. This observation suggests that the factors influencing multilayered film assembly could also promote the formation of the uniform ridges during membrane fabrication.

In CA/NU-1000-0 and CA/NU-1000-10 images, the presence of NU-1000 MOF is well distinguished by its characteristic prism form, as already observed by SEM micrograph images and 3D X-ray microscopy. Importantly, the corresponding phase images shown in Fig. 9d reveal no discernible contrast in the elevated surface regions, attributed to the presence of MOF particles. This absence of contrast in phase images

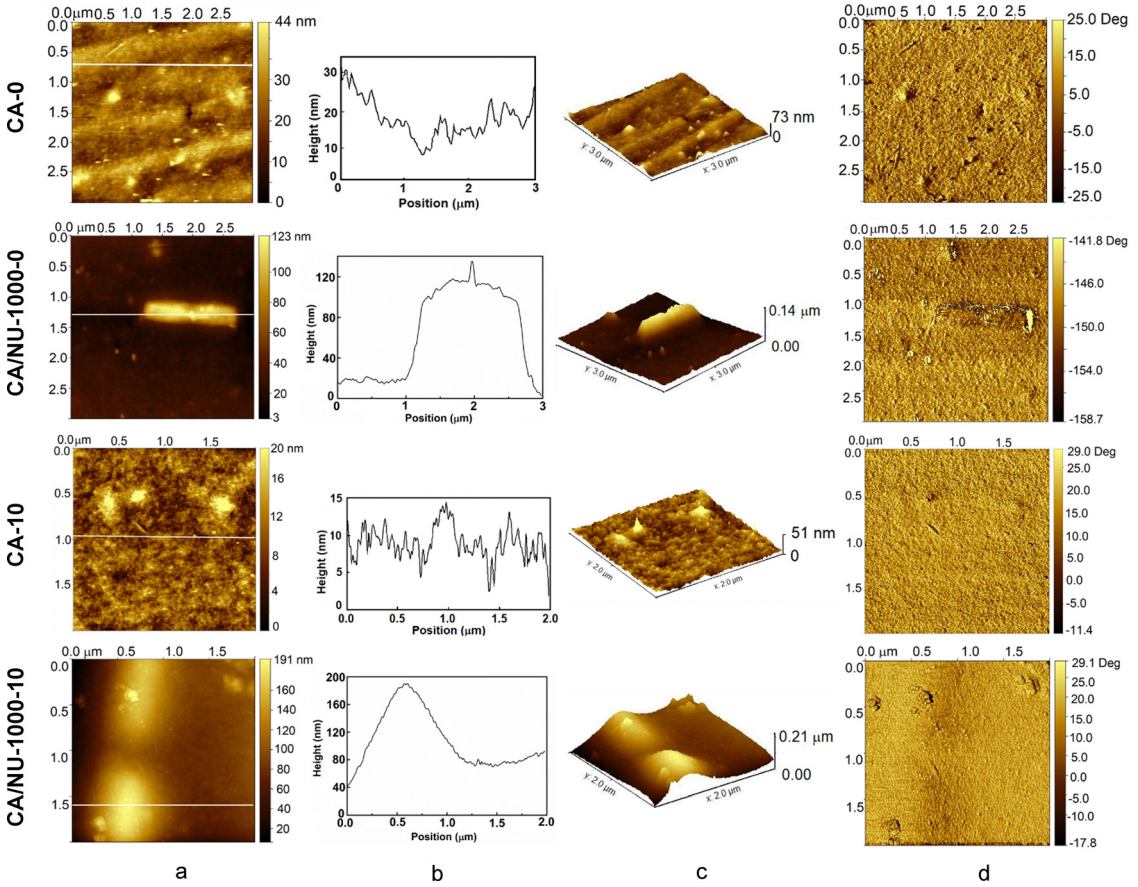

Fig. 9 AFM analysis of the active layer surfaces of CA-0, CA/NU-1000-0, CA-10, and CA/NU-1000-10 membranes: (a) 2D topography images; (b) height profiles taken at the indicated positions; (c) 3D topography images; and (d) phase images. For CA-0 and CA/NU-1000-0, scan area = 3 μm × 3 μm; for CA-10 and CA/NU-1000-10, scan area = 2 μm × 2 μm.

suggests uniform surface properties, *i.e.*, the viscoelastic and adhesive properties at the surface are not altered. Consequently, it can be inferred that NU-1000 particles are effectively covered by a continuous layer of CA polymer, which spreads homogeneously across the active layer surface of the membrane. This polymeric protective layer over NU-1000 MOF particles can play an important role in enhancing MOF stability because these membranes need to be stored in deionized (DI) water, and one of the major drawbacks of MOFs is their poor stability in aqueous environments. Thus, although NU-1000 has good water stability due to the Zr_6-oxo nodes present in its structure,[52] this CA protective layer on top of MOF can not only mitigate the natural degradation of MOF in aqueous solutions but also prevent the MOF leaching from the membrane.

In CA/NU-1000-0 and CA/NU-1000-10 images, the line profiles traced across the regions where MOF particles are present (Fig. 9b) show that they have a length of approximately 2 μm (from CA/NU-1000-0) and a diameter or long diagonal distance of approximately 1 μm (from CA/NU-1000-10), corroborating results seen in the SEM images in Fig. 3e and the data obtained from the 3D CT-scans (Fig. 8d).

Table 1 shows the root-mean-square (RMS) roughness of the membranes' active layer surface obtained from 10 μm × 10 μm AFM topography images. As expected, the presence of NU-1000 increases the membranes' surface roughness, as indicated by the larger RMS roughness values found for CA/NU-1000-0 and CA/NU-1000-10, when compared with the membranes with no MOF particles. It should be noted that the RMS roughness of CA/NU-1000-0 is even higher than that of CA-0, whose surface exhibits fairly regular elevated stripes, as mentioned before. In addition, CA/NU-1000-0 presents an RMS value of 9.9 nm, while the RMS roughness of CA/NU-1000-10 is 12.5 nm.

Table 1 RMS roughness values of the active layer surfaces obtained from 10 μm × 10 μm and 1 μm × 1 μm AFM topography images. Values for 1 μm × 1 μm scans in CA/NU-1000 membranes correspond to "Out-of-MOF" regions

	RMS roughness [nm]	
Membrane	10 μm × 10 μm scans	1 μm × 1 μm scans
CA-0	7.956	5.2 ± 0.4
CA/NU-1000-0	9.908	2.7 ± 0.2[a]
CA-10	6.048	2.7 ± 0.9
CA/NU-1000-10	12.460	4.4 ± 0.4[a]

[a] Averaged values from eight 1 μm × 1 μm scans in "Out-of-MOF" regions.

This variation in roughness values may be attributed to differences in the spatial distribution, orientation, and embedding depth of the NU-1000 particles within the membranes. While in some regions the NU-1000 particles may be closer to the membrane surface, leading to increased surface roughness, in others, although the particles should still be near the surface, they may be more embedded within the polymer matrix, resulting in a smoother topography and lower roughness values.

By comparing the roughness values extracted from 1 μm × 1 μm "Out-of-MOF" regions in CA/NU-1000-10 with those calculated for scans of the same magnitude in CA-10 images (Table 1), it can be concluded that the introduction of NU-1000 in the casting solution matrix does not affect significantly the CA polymer outer layer roughness. At variance, a higher roughness than that of CA/NU-1000-0 is found for CA-0. This higher roughness found for CA-0 reflects the presence of the elevated stripes evidenced at the 10 μm × 10 μm scans.

Fig. 10 shows the topography and phase AFM images, together with height profile plots taken at the indicated positions, of the four membrane surfaces obtained for 500 nm × 500 nm scan areas, where the scans were in "Out-of-MOF" regions for the CA/NU-1000-0 and CA/NU-1000-10 membranes. Membranes CA-0 and CA-10 were prepared using the same casting solution. However, while CA-0 was submerged into the DI water bath immediately after casting, CA-10 was submerged after a solvent evaporation time of 10 seconds. The images show that the CA-0 surface presents larger agglomerates and that they are arranged in a less regular structure than in CA-10. This suggests that the CA polymer chains in CA-0 did not have time to organize and, therefore, when in contact with water, it solidifies instantaneously, leading to the formation of an irregular structure. In contrast, the 10 seconds of evaporation time implemented for CA-10 allowed some acetone to evaporate and promoted the organization of CA polymer chains into homogeneous densely packed polymer layers. Variations in surface morphology can also be observed when comparing CA/NU-1000-0 and CA/NU-1000-10. Here, the images show that the increment in the evaporation time led to a more homogeneous surface where the agglomerates appear more interconnected.

The AFM results show that the superficial CA layer covers NU-1000 uniformly at the membrane surface, allowing the particles to retain their morphology without visible changes

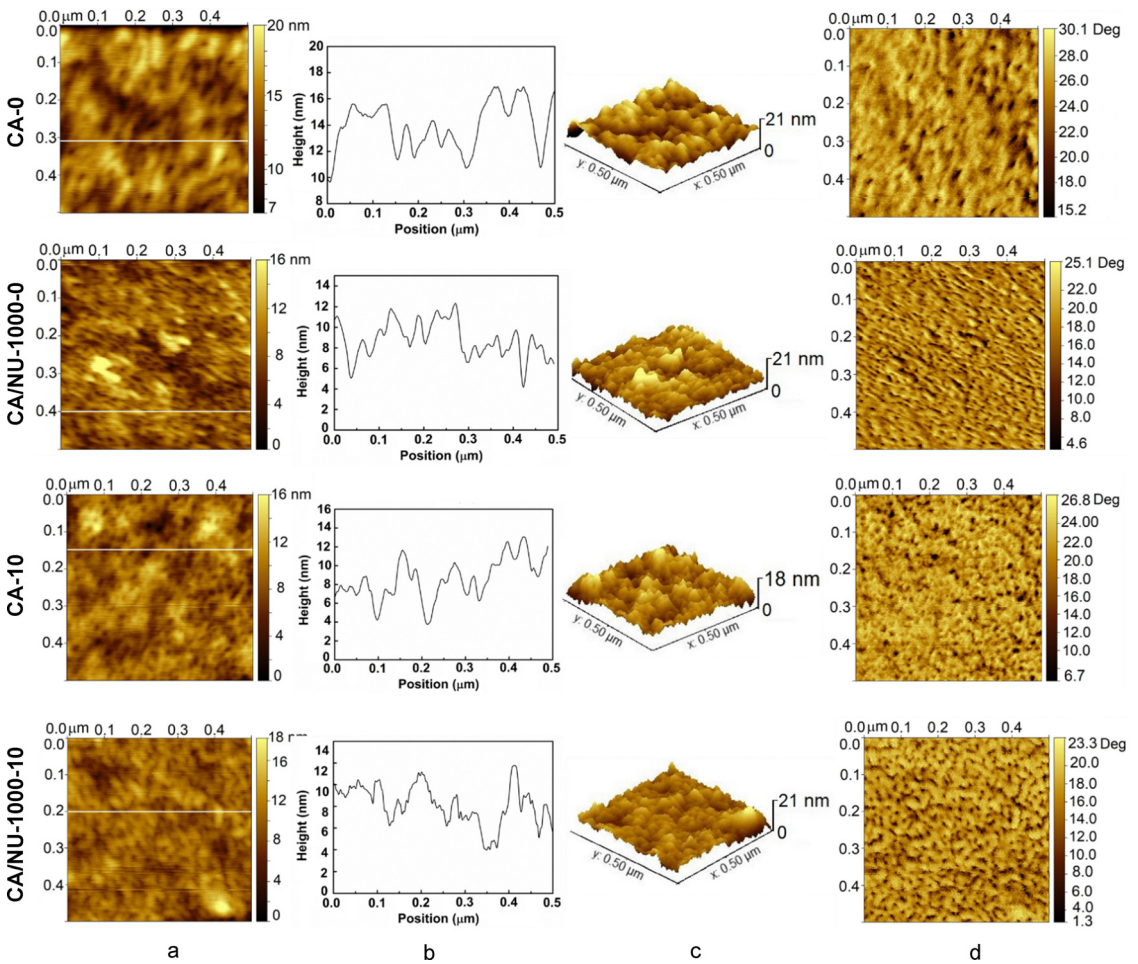

Fig. 10 AFM analysis of CA-0, CA/NU-1000-0, CA-10, and CA/NU-1000-10 membranes in "Out-of-MOF" regions: (a) 2D topography images (500 nm × 500 nm scan area); (b) height profiles; (c) 3D topography images; and (d) phase images.

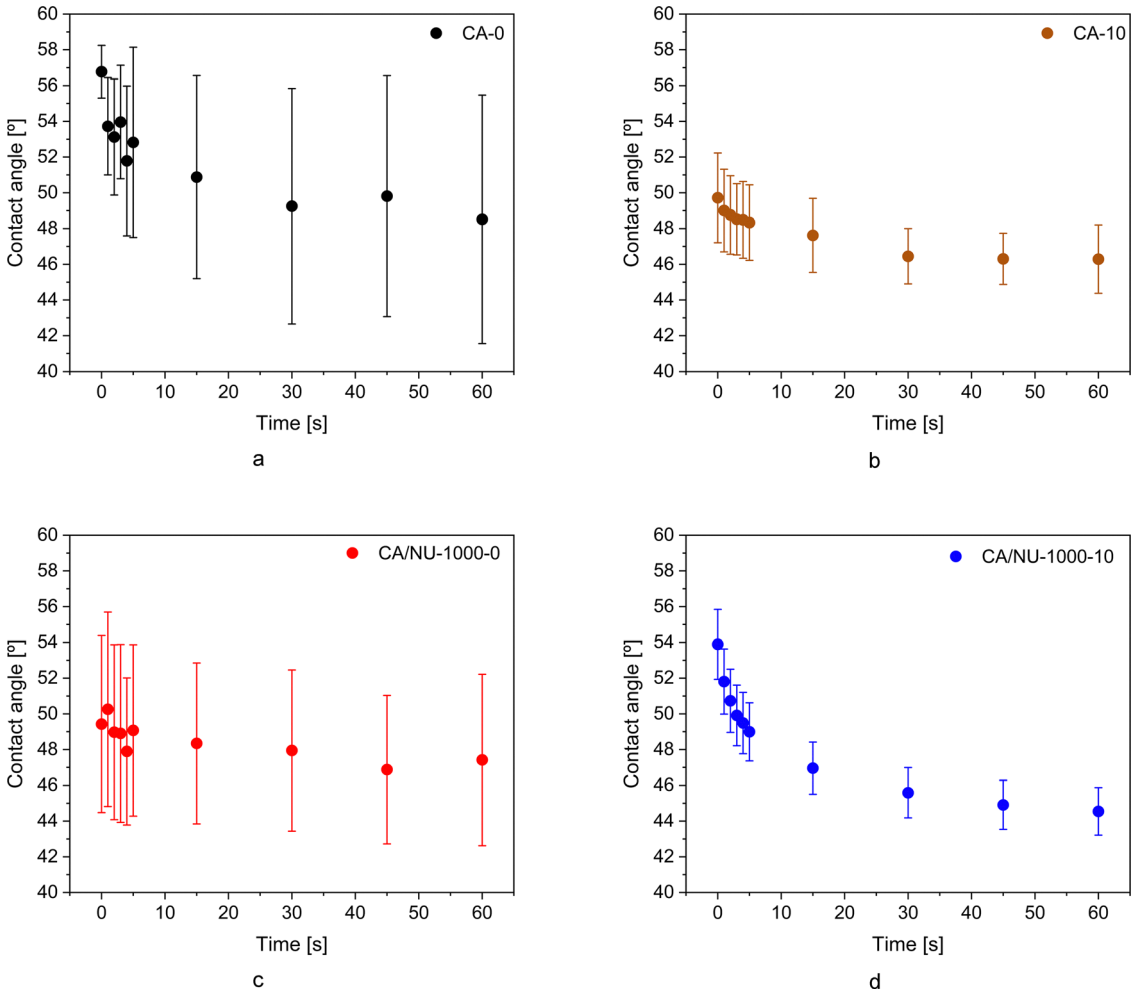

Fig. 11 Evolution of the water contact angle (°) on the active layer surface of the (a) CA-0; (b), CA-10; (c) CA/NU-1000-0; and (d) CA/NU-1000-10 membranes.

and indicating that the continuous polymer layer contributes to the surface stability of the embedded MOF.

2.3.5. Surface wettability by water contact angles. Fig. 11 shows the water contact angles measured on the active layer surface of the CA-0, CA-10, CA/NU-1000-0, and CA/NU-1000-10 membranes as a function of time (60 seconds). At $t = 0$ seconds, the contact angles were 56.8° ± 1.5 (CA-0), 49.7° ± 2.5 (CA-10), 49.4° ± 4.9 (CA/NU-1000-0), and 53.9° ± 2.0 (CA/NU-1000-10). Statistical analysis revealed significant differences between CA-0 and CA-10 ($p < 0.001$) and between CA-10 and CA/NU-1000-10 ($p < 0.001$), while no difference was found between CA-0 and CA/NU-1000-0; a slight difference was observed between CA/NU-1000-0 and CA/NU-1000-10 ($p = 0.011$).

After approximately 1 minute of contact between the sessile water drop and the active layer surface of the membranes, the average contact angles tended to a stationary value of 48.5° ± 7.0 for CA-0 membrane, 46.3° ± 1.9 for the CA-10 membrane, 47.7° ± 4.8 for the CA/NU-1000-0, and 44.5° ± 1.3 for the CA/NU-1000-10 membrane. This stationary phase was observed after the first 30 seconds, when all membranes suffered a sudden decrease in the contact angle. These differences in the contact angle are not statistically significant, which indicates that the evaporation time and the incorporation of the NU-1000 did not interfere with the hydrophilic properties of the membranes. Since all contact angles measured at both 0 and 60 seconds remained below 60°, the membranes can be considered hydrophilic, and the two factors in study did not compromise this property.

Similar results were reported for CA-based membranes using 30 seconds of evaporation (CA-30), where the addition of small amounts of silicon dioxide precursor (0 and 5 wt% SiO_2) to the composition also did not cause significant changes, as observed in this work.[51] It is worth noting that in the same study a significant change in contact angle was only observed when higher amounts of SiO_2 (11 and 18 wt%) were incorporated, whereas, in our case, the added solid content did not exceed 2 wt%. Faria *et al.*[51] reported a water contact angle after 1 minute for pure CA membranes with a 30 second evaporation time of approximately 52°, slightly higher than the values obtained in this work. This small difference, always below 6°, reinforces the observation that such modifications do not significantly impact the surface hydrophilicity. These consistently

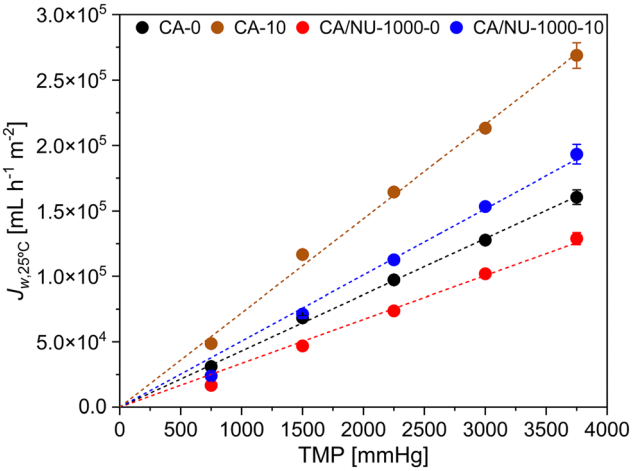

Fig. 12 Pure water fluxes at 25 °C ($J_{w,25°C}$) at different transmembrane pressures (TMPs) for CA-0 (black dots), CA-10 (brown dots), CA/NU-1000-0 (red dots), and CA/NU-1000-10 (blue dots).

low contact angles confirm the hydrophilic nature of the material, attributed to the hydroxyl and acetyl functional groups present in the CA polymer, which enable interactions with water molecules.

2.3.6. Permeation properties. The permeation performance of the CA-0, CA/NU-1000-0, CA-10, and CA/NU-1000-10 membranes was assessed by measuring their hydraulic permeability (L_p) and molecular weight cut-off (MWCO). L_p values obtained from linear correlations between pure water fluxes (J_w) and transmembrane pressure (TMP), shown in Fig. 12, were: 43.0, 33.5, 72.0 and 50.5 mL h^{-1} m^{-2} mmHg^{-1} for CA-0, CA/NU-1000-0, CA-10, and CA/NU-1000-10, respectively. The presence of NU-1000 decreased the L_p and, contrary to what was expected, L_p was higher for higher solvent evaporation times. A possible explanation for this is that there needs to be some time for acetone (the more volatile solvent) to evaporate and properly form the active dense layer. This also increases the viscosity of the casting solution before it enters the coagulation bath, slowing down the exchange between formamide and water and resulting in larger pores and, consequently, a higher L_p.

The rejection coefficients to solutes of increasing molecular weight for all four membranes reflected MWCO values of 7 kDa for the CA-0 and CA/NU-1000-0 membranes, and 26 kDa and

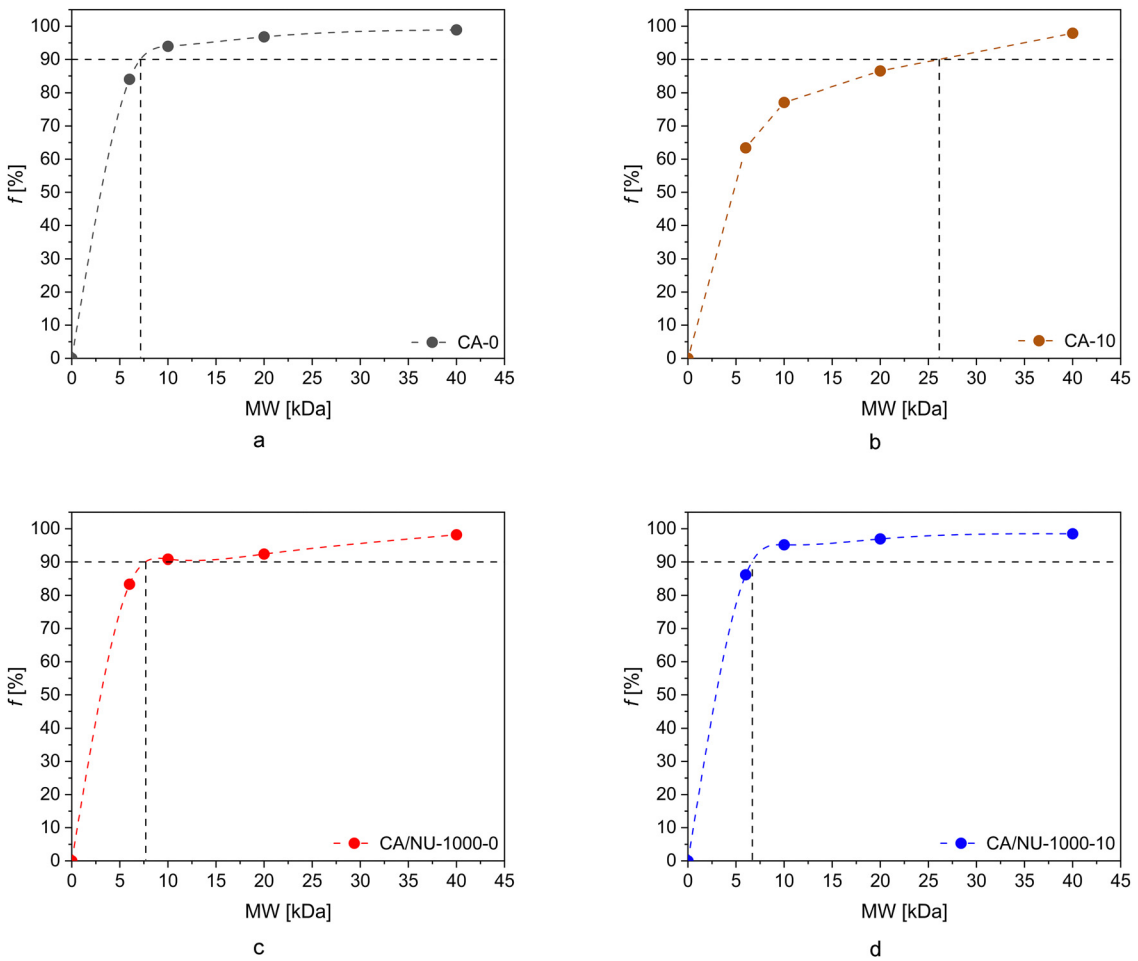

Fig. 13 Rejection coefficient profiles to solutes of increasing molecular weight for: (a) CA-0; (b) CA-10; (c) CA/NU-1000-0; and (d) CA/NU-1000-10 membranes.

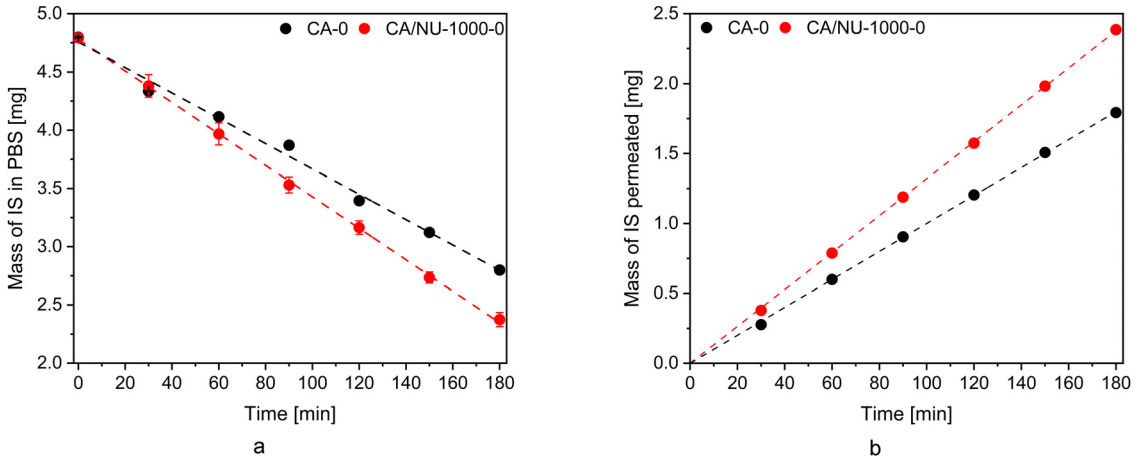

Fig. 14 Clearance of indoxyl sulfate (IS) from PBS by the CA-0 (black dots) and CA/NU-1000-0 (red dots) membranes in terms of: (a) mass of IS in the PBS (feed solution) *vs.* time; and (b) the mass of IS in the permeate *vs.* time.

7 kDa for the CA-10 and CA/NU-1000-10 membranes, respectively (Fig. 13). These values fall in the range of HD membranes and ensure the permeation of small UTs, such as urea, creatinine, and free IS, as well as the retention of essential proteins, such as HSA.

2.4. Clearance of indoxyl sulfate by the CA and CA/NU-1000 membranes from phosphate-buffered saline

The removal of IS from a PBS/IS solution by the CA/NU-1000-0 membrane was evaluated by circulating a 2.0 mg dL^{-1} solution of IS in PBS through the system described in Section 4.7 (Experimental section). Flat sheet membrane modules (FSMMs) containing samples of the CA/NU-1000-0 membrane (total surface area of 35.88 cm^2), were operated for 180 minutes at a TMP of 97.5 mmHg. For comparison purposes, a similar experiment was performed in the absence of NU-1000 MOFs, with FSMMs containing samples of the CA-0 membrane.

Fig. 14a and b show the mass of IS in the IS/PBS solution (feed) and in the permeate throughout 180 minutes, respectively, for both experiments. Fig. 14a shows that the mass of IS in the feed solutions of both experiments at t = 0 minutes was 4.79 mg, which decreased linearly with time, reaching the lowest values, at t = 180 minutes, of 2.37 mg and 2.79 mg for the CA/NU-1000-0 and CA-0 membranes, respectively. Fig. 14b shows that the amount of IS that permeated the CA/NU-1000-0 and CA-0 membranes was 2.39 and 1.79 mg, respectively, indicating that the presence of NU-1000 MOFs increased the permeation of IS by a factor of 1.3. Results also indicate that, in contrast to what was observed for the adsorption studies of IS by NU-1000 in PBS (Section 2.2), IS is not irreversibly adsorbed by the MOFs but, instead, their presence in the CA/NU-1000-0 membrane promotes the clearance of IS from the feed solution into the permeate.

In the pristine CA membrane, IS transport occurs by diffusion through the dense selective layer, resulting in permeation across the membrane. In contrast, CA/NU-1000-0 MMMs combine diffusion with reversible adsorption of IS onto NU-1000 within the membrane matrix. These adsorption–desorption interactions enhance IS partitioning within the membrane, promoting diffusion and leading to increased permeation compared to the control membrane under identical operating conditions.

Kim *et al.*[53] fabricated double-layer MMMs incorporating AC and compared their performance with three commercial dialysis membranes. Their assays were performed using IS-spiked plasma at ~4.0 mg dL^{-1} for 4 hours, where most IS is in bound form. Under these conditions, they reported removals of 500 ± 176 mg m^{-2} for AC-based MMMs and an average of ~340 mg m^{-2} for the commercial membranes. In our study, IS was only in free form in buffered solution at ~2.0 mg dL^{-1}, with a shorter permeation time of 3 hours, and the CA/NU-1000-0 membrane removed 666 mg m^{-2} of IS. A direct comparison is not entirely appropriate, since their assays used plasma while ours used buffered solution, their formulation contained 60 wt% AC relative to the total polymer mass whereas our membranes incorporated only 2 wt% NU-1000 (30-times less adsorptive particles incorporated), and their experiments take one hour longer. Considering these differences and the limitations of the comparison, the CA/NU-1000-0 membrane demonstrates promising clearance.

Overall, these findings demonstrate that the incorporation of NU-1000 into the CA matrix enhances IS removal under crossflow conditions, while maintaining the accessibility of the MOF active sites within the membrane during filtration.

3. Conclusions

NU-1000 was successfully synthesized and exhibited the expected structural, chemical, and morphological properties. In buffered IS solution, NU-1000 removed ~53% of IS within 180 minutes, demonstrating its strong adsorption capacity and supporting its potential for PBUT targeting. Based on these results, mixed matrix membranes (MMMs) composed of cellulose acetate (CA) and NU-1000 (CA/NU-1000) were fabricated by phase inversion to

combine CA processability with the adsorption capability provided by the Zr-based metal–organic framework (MOF). NU-1000 microcrystals were uniformly embedded and surface-covered by CA, as confirmed by SEM/EDS, ATR-FTIR, AFM, and 3D X-ray microscopy, which also revealed asymmetric cross-sectional morphology with a dense skin and porous sublayer, without compromising hydrophilicity (contact angles $<60^{\circ}$) or introducing surface defects. These structural attributes translated into ultrafiltration (UF) performance within the range of values typically found for hemodialysis membranes (MWCO of $\sim$7 kDa for CA-0 and CA/NU-1000-0; L_p of 43.0 and 33.5 mL h^{-1} m^{-2} $mmHg^{-1}$ for CA-0 and CA/NU-1000-0, respectively), enabling the passage of water and small solutes.

Under crossflow conditions, CA/NU-1000-0 membranes increased IS transport by a factor of 1.3 relative to CA-0. This behavior is attributed to adsorption-assisted transport, where reversible interactions between IS and NU-1000 enhance solute partitioning within the membrane and promote diffusion across the selective layer, resulting in increased permeation.

Collectively, these results demonstrate that CA/NU-1000 MMMs preserve the key transport and structural properties of CA membranes while introducing MOF-driven adsorption that enhances solute transport. This approach provides a promising basis for improving PBUT clearance in hemodialysis through adsorption-assisted transport mechanisms. Future work should explore long-term stability, potential leaching, and the removal of PBUTs in their protein-bound form.

4. Experimental section

4.1. Materials

All chemicals were used as received without further purification. 1,3,6,8-Tetrabromopyrene ($C_{16}H_6Br_4$, purity $\geq$98%) and 4-(methoxycarbonyl)-phenylboronic acid ($C_8H_9BO_4$) were supplied by Tokyo Chemical Industry (TCI). Potassium phosphate tribasic (K_3PO_4, purity $\geq$98%), tetrakis-(triphenylphosphine)-palladium ($Pd(PPh_3)_4$, purity $\geq$99%), cellulose acetate (CA, average Mn $\sim$30 000 by GPC) and indoxyl sulfate (IS) were acquired from Sigma-Aldrich (St. Louis, MO, USA). Chloroform ($CHCl_3$, analytical reagent grade), *N*,*N*-dimethylformamide (DMF, anhydrous, solvent synthesis grade), hydrochloric acid (HCl, 37%, analytical reagent grade) and dioxane ($C_4H_8O_2$, analytical reagent grade) were provided by Fisher Scientific (Merelbeke, Belgium). Potassium hydroxide (KOH, purity $\geq$85%) was provided by ACROS Organics. Acetonitrile (HPLC grade), ammonia solution 30% (for analysis ACS), *n*-hexane (HPLC grade) and formic acid 99% (for analysis ACS) were purchased from Carlos Erba (Val-de-Reuil, France). Pure acetone was purchased from José Manuel Gomes dos Santos, Lda (Odivelas, Portugal). Zirconium chloride octahydrate ($ZrOCl_2{\cdot}8H_2O$, purity of 98%) and propan-2-ol, were purchased from Thermo Scientific™ (Waltham, MA, USA). Polyethylene glycol (PEG) with different molecular weight (MW), PEG 6000 (MW 6000 g mol^{-1}) and PEG 10 000 (MW 10 000 g mol^{-1}) were purchased from Merck, Schuchardt oHG (Hohenbrunn, Germany), while PEG 20 000 (MW 20 000 g mol^{-1}) was purchased from Alfa Aesar (Kandel, Germany). Dextran T40 (MW 40 000 g mol^{-1}), potassium dihydrogen phosphate ($\geq$99.5%), sodium chloride ($\geq$99.5%) and disodium hydrogen phosphate dihydrate ($\geq$99.5%) were all acquired from Merck (Darmstadt, Germany). Formamide (for analysis ACS), benzoic acid (C_6H_5-COOH, purity $\geq$99.5%) and potassium chloride ($\geq$99.5%) were acquired from PanReac Applichem (Barcelona, Spain).

4.2. Synthesis and characterization of NU-1000 MOFs

The synthesis of the metal–organic framework (MOF) NU-1000 followed the protocol described by Wang *et al.*[35] Briefly, after the preparation of tetraethyl 4,4′,4″,4‴(-pyrene-1,3,6,8-tetrayl)-tetrabenzoate (H_4TBAPy), zirconyl chloride octahydrate and benzoic acid were mixed at 80 °C for 1 hour in DMF. Then, H_4TBAPy was added to the solution, and the mixture was sonicated to ensure proper dispersion of the organic linker. The mixture was left in the oven for 15.5 hours at 100 °C, resulting in a light-yellow powder. The mixture was centrifuged,

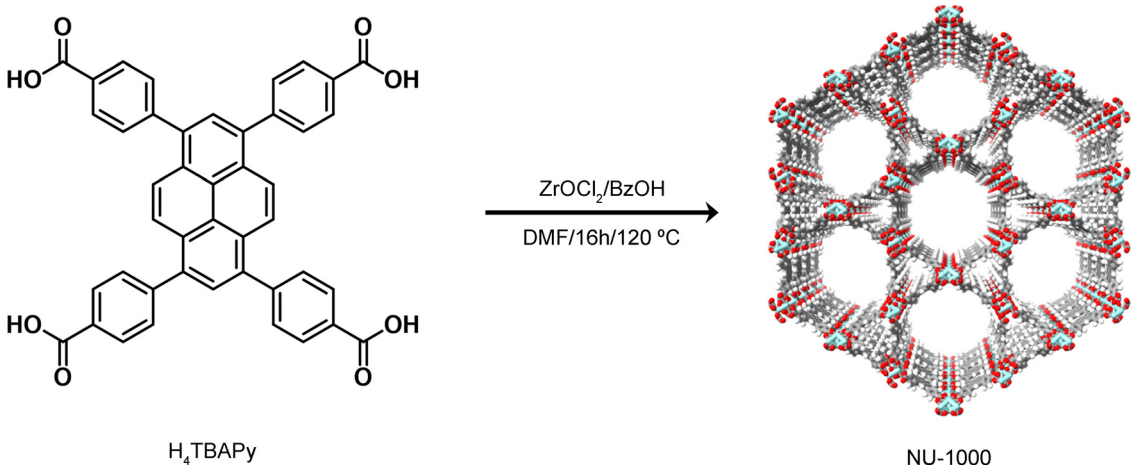

Fig. 15 Crystallographic representation of NU-1000 showing the arrangement of Zr_6 clusters and TBAPy linkers and the resulting hexagonal mesoporous channels.

the solid was collected and then dispersed in DMF. HCl 8 M was then added to the solution, and the mixture was left in the oven at 100 °C for 12 hours. After this, the mixture was centrifuged and DMF was added to the recovered solid. The mixture was centrifuged again, and acetone was added to the solid for 12 hours. Finally, the mixture was centrifuged, and the solid powder was placed in a vacuum oven at 80 °C for 1 hour (Fig. 15). Prior to any experiment, NU-1000 was activated at 120 °C for 12 hours, following previously reported protocols.[36,54]

The NU-1000 MOF was characterized by ATR-FTIR in an Agilent Cary 630 spectrometer, TGA was performed in a Perkin-Elmer Thermal Analyzer and PXRD studies were performed with a Bruker D8 Advance powder diffractometer coupled to a SSD160 detector using copper radiation (Cu Kα, λ = 1.5406 Å) and a nickel filter. Nitrogen adsorption–desorption studies were carried out using an Accelerated Surface Area and Porosimetry System (ASAP ®2060) at 77 K, and the pore size distribution was determined using the Barrett–Joyner–Halenda (BJH) method. SEM and EDS were performed in a Thermo Scientific Phenom ProX G5 Desktop SEM. The length of the NU-1000 MOFs was calculated from measurements using the ImageJ software (version 2.3.0) on 20 different MOFs identified in micrographs with 3000× amplification.

4.3. *In silico* studies

Molecular docking studies were performed using HEX 8.0.0 software and visualization was performed using Discovery Studio 3.5 software. The parameters used for docking include correlation type shape only, FFT mode 3D, grid dimension 0.6, receptor range 180, ligand range 180, twist range 360, distance range 40.

4.4. Adsorption of indoxyl sulfate by NU-1000 MOFs in phosphate-buffered saline

Fig. 16 shows a schematical representation of the experimental setup used to evaluate the adsorption of IS by the NU-1000 MOFs. First, IS/PBS solution with concentration 2.0 mg dL^{-1} (10 mL) was added to six 50 mL conical sterile polypropylene centrifuge tubes. Then, NU-1000 MOFs (6 mg) were added to three of the tubes, while the other three were left only with the IS/PBS solution (negative control). All six tubes were placed horizontal-wise in a mechanical shaker, CAT Shaker S50 (Ingenieurbüro CAT, M. Zipperer GmbH, Germany), and kept under gentle agitation at room temperature. The experiment was carried out for 3 hours. At each of the 3 hours, two tubes were removed from the shaker, one with NU-1000 MOFs and another from the negative control, and centrifuged at 850 g for 5 minutes in a 5810 R centrifuge (Eppendorf Ibérica S.L.U, Spain) to allow the NU-1000 MOFs to settle at the bottom of the conical tubes. The supernatant was collected and analyzed to obtain the concentration of IS. This experiment was performed in duplicate. Quantification of IS was performed by a modified version of the protocol by Tao *et al.*[4] and analyzed by high performance liquid chromatography (HPLC) using Waters HPLC system series 2695 (Waters, Milford, MA) equipped with an autosampler, Empower software data station, version 2.0.7, and a multi fluorescence detector (2475 module). A detailed description can be found in SI (Section 1.1).

4.5. Fabrication of CA and CA/NU-1000 membranes

Two MMMs, CA/NU-1000-0 and CA/NU-1000-10, each containing 2 wt% NU-1000 MOFs, were prepared *via* the phase inversion method. Casting solutions were prepared by first mixing CA (4 g), formamide (4.25 g), and acetone (11.29 g) in a glass vial. The solution was mechanically agitated in a CAT Shaker S50 for 4 hours at room temperature until complete dissolution of CA. Subsequently, NU-1000 MOFs (80 mg) were dispersed in formamide (4.04 g) which was added dropwise to the CA solution. The vial was sealed and mechanically agitated for 20 hours at room temperature. The resulting solutions were cast onto glass plates at room temperature using a 250 μm

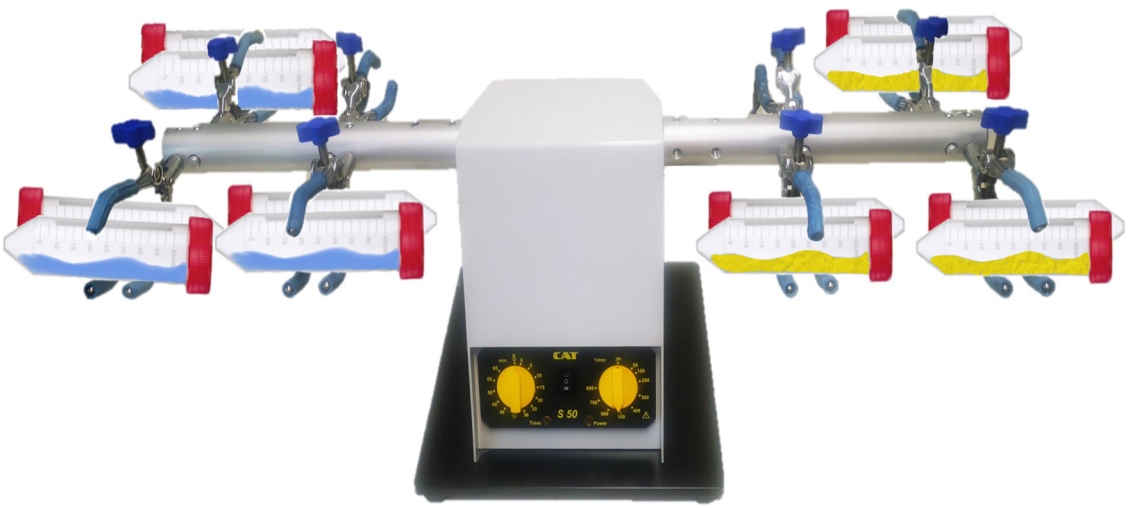

Fig. 16 Schematic representation of the experimental setup used to evaluate the adsorption of indoxyl sulfate (IS) when placed in direct contact with NU-1000 MOFs (shown in yellow on the right). As a negative control, the same IS/PBS solution was kept under the same conditions but without the NU-1000 MOFs (shown in blue on the left).

Gardner knife and immersed in a coagulation bath of cold DI water (3 °C) after solvent evaporation times of 0 or 10 seconds, yielding CA/NU-1000-0 and CA/NU-1000-10 membranes, respectively. After 24 hours in the coagulation bath, membranes were removed and stored in DI water at 4 °C until further use. For comparison purposes, two pure polymer membranes, CA-0 and CA-10, were prepared using the same procedure and solvent evaporation times, but without NU-1000.

4.6. Characterization of CA and CA/NU-1000 membranes

4.6.1. Drying of the CA and CA/NU-1000 membranes. Samples of the CA and CA/NU-1000 membranes (3 cm × 3 cm) were dried by a solvent exchange method, following the procedure reported by Lui *et al.*[55] Briefly, membranes were immersed in a set of solvent mixtures composed of DI water, propan-2-ol and *n*-hexane for at least 24 hours in each of the mixtures. The solvent solution sequence was: (1) 100% DI water, (2) 66% DI water and 33% propan-2-ol, (3) 33% DI water and 66% propan-2-ol, (4) 100% propan-2-ol, (5) 66% propan-2-ol and 33% *n*-hexane, (6) 33% propan-2-ol and 66% *n*-hexane, and (7) 100% *n*-hexane. After the complete evaporation of *n*-hexane, the membranes were stored at room temperature in a desiccator.

4.6.2. Membrane morphology by scanning electron microscopy and surface chemistry by energy-dispersive X-ray spectroscopy. Samples of the dried membranes were fractured following immersion in liquid nitrogen, placed on an aluminum stub using double-sided carbon tape and sputter coated (15–25 seconds) with a thin Au/Pd film in a coater (Quorum Technologies, model Q150T ES). SEM and EDS analysis was carried out using a Thermo Scientific™ Phenom™ ProX G6 desktop SEM (Thermo Scientific™, Waltham, MA, USA). SEM images were taken of the dense active layer, porous surface and cross-sections of the CA-0, CA/NU-1000-0, CA-10, and CA/NU-1000-10 membranes. The total thickness of the membranes was calculated from measurements using the ImageJ software (version 2.3.0) in six different regions of the cross-section micrographs of each membrane. The area (%) of the active surface of the CA/NU-1000 membranes occupied by the NU-1000 MOFs was found from measurements on 3 different SEM images of each membrane (3000× magnification) using the ImageJ software (version 2.3.0).

4.6.3. Chemical composition by attenuated total reflectance – Fourier transform infrared spectroscopy. ATR-FTIR analysis of the dried CA-10 and CA/NU-1000-10 membrane samples was performed by a PerkinElmer Frontier FT-IR spectrometer (Waltham, MA, USA), using a Pike Miracle Single Reflection ATR sampling accessory from Pike Technologies with a Ge crystal (Graseby Specac, Smyrna; sampling depth: 0.2–1.1 μm at 4000–730 cm^{-1}). Each spectrum was obtained by averaging 264 scans with a resolution of 4 cm^{-1}.

4.6.4. Internal structure of CA/NU-1000-10 by 3D X-ray microscopy. Dried CA/NU-1000-10 samples with a total volume of 0.12 mm^3 were analyzed using an X-ray nanotomograph (SkyScan 2214, Bruker, Belgium) to obtain a 3D reconstruction of their internal structure. Image acquisition over a total volume of interest of 0.05 mm^3 was performed with a tungsten-source X-ray tube operated at 75 kV and 180 μA, without a filter. Scans were acquired for 2 hours, 57 minutes and 14 seconds at a voxel size of 0.6 μm, with samples rotated through 180° in increments of 0.15°. Each projection was captured with an exposure time of 1800 milliseconds, using a frame averaging of three. No binning was applied, and a CCD detector was used.

CT reconstruction was performed with NRecon software (version 2.2.0.6, Bruker) using the Feldkamp algorithm. A representative region of interest (ROI) was selected in CTAn software (version 1.20.8.0, Bruker), followed by image binarization to highlight the structures of interest in white. Quantitative analyses of NU-1000 particles and void sizes, as well as spatial resolution, were carried out using the 3D plug-in. The length of the NU-1000 particles and the diameter of the membrane voids were determined using a sphere-fitting algorithm, which fits a sphere to the medial axis of each feature to calculate its size, using a lower threshold of 127. For the determination of the membrane porosity, after the delimitation of the ROI, a contrast enhancement filter (3D space) was applied to increase contrast, followed by the use of the automatic Mid-Range threshold. To determine the total thickness, the membrane was considered as a single object. Volume rendering was performed with CTVox software (version 3.3.1, Bruker).

4.6.5. Surface topography by atomic force microscopy. The topography of the active layer surface of the dried samples of the CA-0, CA/NU-1000-0, CA-10, and CA/NU-1000-10 membranes was investigated by AFM using a Nano Observer microscope from Concept Scientific Instruments (Les Ulis, France), operating in tapping mode. The tips consisted of silicon probes with tip radius <10 nm and resonance frequency between 200 and 400 kHz (APPNano, model: ACT). All images were acquired with a resolution of 512 × 512 pixels and processed with Gwyddion (version 2.56) software.

4.6.6. Surface wettability by water contact angles. The hydrophilicity of the CA-0, CA/NU-1000-0, CA-10, and CA/NU-1000-10 membranes was evaluated by water contact measurements using the sessile drop technique. Microdrops (volume ~5 μL) of water produced with a micrometric syringe were deposited on the active layer surface of each membrane at room temperature. A video camera (model JAI CV-A50) mounted on a microscope (Leica MZ) and connected to a frame grabber (Data Translation model DT3155) recorded a sequence of images over a period of 1 minute. The ADSA-P software (Axisymmetric Drop Shape Analysis-Profile, Applied Surface Thermodynamics Research Associates, Toronto, Canada) was used for image acquisition and analysis. Results of water contact angles are expressed as the contact angle (average ± SD) derived from at least ten measurements on distinct areas of each membrane.

Descriptive statistics and inferential analysis were performed using IBM SPSS Statistics v30 (SPSS Inc., Chicago, IL). A significance level of 0.05 (95% confidence) was used for the statistical analysis. First, data normality within each group was evaluated using the Kolmogorov–Smirnov and Shapiro–Wilk tests, and the assumption of normality was confirmed in both.

Homogeneity of variances was then assessed using Levene's test. Since variance heterogeneity was detected, Welch's ANOVA was applied under the null hypothesis (H0) that all group means are equal, followed by a Games–Howell *post hoc* test.

4.6.7. Permeation performance. The permeation properties of the CA-0, CA/NU-1000-0, CA-10, and CA/NU-1000-10 membranes were evaluated in terms of L_p and MWCO using a laboratory crossflow UF setup which has been previously described.[56,57] Briefly, the setup is composed of a feed tank with approximately 5 L of capacity, a three-phase induction pump which pressurizes the UF system and controls the feed flow rate through a series of five permeation cells, each with an effective membrane area of 17.35 cm^2. The operating gauge pressure, controlled by a back-pressure valve, was determined as the average values at the inlet and outlet manometers positioned before and after the series of permeation cells. To reduce pressure fluctuations in the cells a surge tank was placed downstream of the pump.

Prior to each test, all membranes were compacted to stabilize their structure and eliminate membrane compaction effects. This was performed by circulating DI water through the setup at a flow rate of 1.8 L min^{-1} and a TMP of 7.0 bar (~40% higher than the highest operating pressure) for a period of 2.5 hours. All UF experiments were conducted at ambient laboratory temperatures (24–28 °C).

L_p was found by the slope of the linear variation of the pure water permeate flux, J_w, as a function of the applied TMP. J_w values were measured at a flow rate between 2.3 and 3.3 L min^{-1}, with TMPs ranging from 1.0 to 5.0 bar, and corrected for 25 °C using the values of relative viscosity and density of pure water.

The apparent rejection coefficients (f), of the membranes to a series of neutral solutes with increasing molecular weights were found and plotted as a function of the MW of each solute to find the MWCO. The solutes used to prepare the solutions were polyethylene glycols with MWs of 6000 Da (PEG 6000), 10 000 Da (PEG 10 000), 20 000 Da (PEG 20 000), and dextran with MW of 40 000 Da (Dextran T40), at a concentration of 1 g L^{-1}. Permeation assays were performed at a flow rate of 3.3 L min^{-1} and at a TMP of 1 bar. Solute concentrations in the permeate and feed solutions were measured, in triplicate, by a total organic carbon analyzer (TOC VCPH/CPN Shimadzu, Japan).

4.7. Clearance of indoxyl sulfate by the CA-0 and CA/NU-1000-0 membranes from phosphate-buffered saline

Fig. 17 shows a schematic representation of the crossflow filtration setup used to evaluate the clearance of IS from PBS by the CA-0 and CA/NU-1000-0 membranes, which has been previously described by Rodrigues *et al.*[58] Briefly, the feed solution circulates from a reservoir to a pulsation damper by a peristaltic pump (ECOLINE VC-360, from ISMATEC, Wertheim, Germany) and through two FSMMs. The FSMM feed channel was designed as a slit-like microchannel, with a height of 400 μm, which is significantly smaller than its width (2.0 cm) and length (7.5 cm). The effective membrane surface area corresponds to the membrane area defined by the O-ring, with each FSMM providing an effective area (A_{eff}) of 17.94 cm^2, resulting in a total effective surface area of 35.88 cm^2. This channel geometry was selected to ensure operation within the shear stress range previously validated for this FSMM design. Integral to this setup are two pressure transducers, P1 and P2 (Deltran®, Utah Medical Products, Midvale, UT, USA), positioned at the FSMM inlet and outlet, respectively. These transducers interface with a data acquisition (DAQ) system, employing a LabView module (National Instruments 9237, TX, USA) to record pressure values. The permeate of the two FSMMs is collected in two separate containers. All the tubing in the

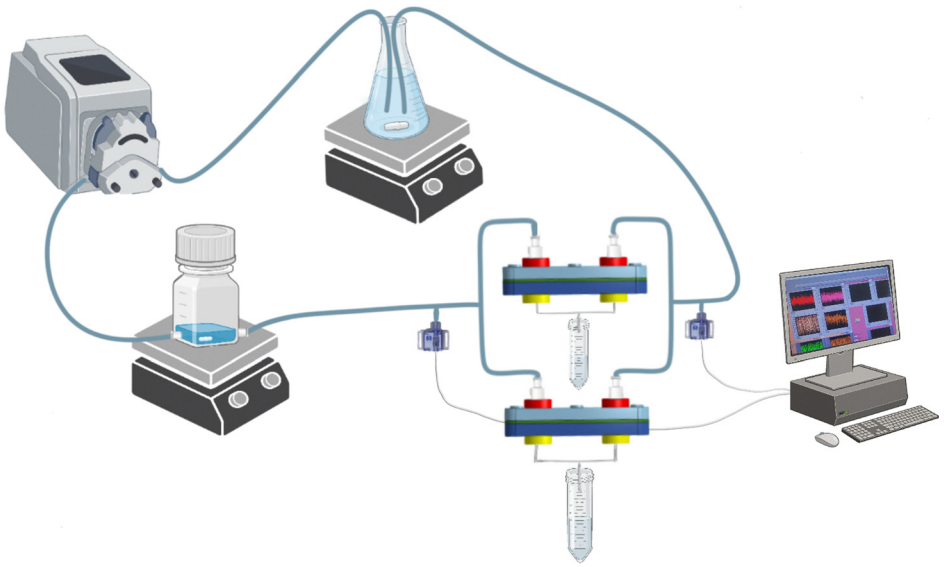

Fig. 17 Schematic representation of the crossflow filtration setup used to evaluate the permeation performance of the CA-0 and CA/NU-1000-0 membranes, operating with two flat sheet membrane modules (FSMMs) in parallel.

Table 2 Operating conditions for the filtration experiments using CA-0 and CA/NU-1000-0 membranes

Parameter	CA-0	CA/NU-1000-0
Initial IS concentration [mg dL^{-1}]	2.0	2.0
Feed volume [mL]	240	240
Flow rate [mL min^{-1}]	53	55
TMP [mmHg]	94.0	97.7
Temperature [°C]	24 ± 1	24 ± 1
Filtration time [min]	180	180
Sampling interval [min]	30	30

circuit is medical grade (Tygon ND-100-65, McMaster, Elmhurst, IL, USA).

To evaluate the clearance of IS from PBS, a 2.0 mg dL^{-1} solution of IS in PBS (240 mL) were introduced into the feed reservoir and circulated through the circuit at an average flow rate of 55 mL min^{-1} and average TMP of 97.5 mmHg for 3 hours at room temperature (24 ± 1 °C). Two samples of the CA/NU-1000-0 membrane, each with an effective surface area of 17.94 cm^2, were placed in the two FSMMs, and samples of the feed solution (IS in PBS) and collected permeate were taken at consistent 30-minute intervals. For comparison purposes, the same experiment was performed with two samples of the CA-0 membrane (total A_{eff} 35.88 cm^2) in the FSMMs, and PBS was circulated at an average flow rate of 53 mL min^{-1} and average TMP of 94.0 mmHg for 3 hours at room temperature (24 ± 1 °C). Both feed and permeate samples were processed through the Salting-out Assisted Liquid–Liquid Extraction (SALLE) method detailed in ref. 59, and the concentration of IS was quantified in triplicate by fluorescence spectroscopy (FP-8500 Spectrofluorometer, Jasco, United Kingdom). Details of the quantification method can be found in SI (Section 1.2).

A summary of the operating conditions used in the filtration experiments for the CA-0 and CA/NU-1000-0 membranes is provided in Table 2.

Author contributions

Conceptualization: M. F.; data curation: R. F. P., B. S. N., F. S. C. R., A. P., A. C. and A. K.; formal analysis: R. F. P., B. S. N., F. S. C. R. and M. F.; funding acquisition: M. F.; investigation: R. F. P., B. S. N., F. S. C. R., A. P., A. C., A. K. and M. F.; methodology: R. F. P., B. S. N., F. S. C. R., A. P., A. C. and A. K.; project administration: M. F.; resources: M. F.; software: R. F. P., F. S. C. R., A. P. and A. C.; supervision: M. F.; validation: R. F. P., F. S. C. R. and M. F.; writing – original draft: M. F., R. F. P. and F. S. C. R.; writing – review and editing: M. F., R. F. P., F. S. C. R., A. P., A. C. and A. K.

Conflicts of interest

The authors declare no conflicts of interest.

Data availability

Additional experimental and methodological details are provided in the supplementary information (SI). Ref. 4 and 59 are cited in the SI. Supplementary information (SI) available. See DOI: https://doi.org/10.1039/d6tb00006a.

Acknowledgements

This work was financially supported by Fundação para a Ciência e a Tecnologia (FCT) *via* LaPMET, Laboratory of Physics for Materials and Emerging Technologies [LA/P/0095/2020]; Research Unit CeFEMA, Centre of Physics, Engineering and Advanced Materials [UID/04540/2025 and UID/PRR/04540/2025]; CEEC Individual Program [CEECIND/CP1651/CT0016]; Exploratory Research Project [2023.12035.PEX (DOI: 10.54499/2023.12035.PEX)]; PhD research grant [UI/BD/150949/2021]; and by FCT/through national funds and, when applicable, co-funded EU funds under Instituto de Telecomunicações [UID/50008/2025 (DOI: https://doi.org/10.54499/UID/50008/2025)]. The authors gratefully acknowledge Luís F. Santos for providing access to the ATR-FTIR equipment, Ana P. Serro for assistance with contact angle measurements, and Sérgio B. Gonçalves for support with the statistical analysis.

References

1 M. Faria and M. N. de Pinho, *Transl. Res.*, 2021, **229**, 115–134.
2 S. Daneshamouz, U. Eduok, A. Abdelrasoul and A. Shoker, *NanoImpact*, 2021, **21**, 100299.
3 S. Lekawanvijit, A. R. Kompa and H. Krum, *Am. J. Physiol.-Ren. Physiol.*, 2016, **311**, F52–F62.
4 X. Tao, S. Thijssen, P. Kotanko, C.-H. Ho, M. Henrie, E. Stroup and G. Handelman, *Sci. Rep.*, 2016, **6**, 23389.
5 M. Madero, K. B. Cano, I. Campos, X. Tao, V. Maheshwari, J. Brown, B. Cornejo, G. Handelman, S. Thijssen and P. Kotanko, *Clin. J. Am. Soc. Nephrol. CJASN*, 2019, **14**, 394–402.
6 X. Tao, S. Thijssen, N. Levin, P. Kotanko and G. Handelman, *Blood Purif.*, 2015, **39**, 323–330.
7 F. S. C. Rodrigues and M. Faria, *Toxins*, 2023, **15**, 110.
8 M. Ghannoum, J. Bouchard, T. D. Nolin, G. Ouellet and D. M. Roberts, *Semin. Dial.*, 2014, **27**, 350–361.
9 C. A. Howell, S. R. Sandeman, Y. Zheng, S. V. Mikhalovsky, V. G. Nikolaev, L. A. Sakhno and E. A. Snezhkova, *Carbon*, 2016, **97**, 134–146.
10 Z. Yue, G. Xiaoli, Z. Juan, W. Qun, W. Feng and Z. Yongke, *Colloids Surf., B*, 2024, **233**, 113655.
11 S. Carro, C. J. Cabello-Alvarado, M. Andrade-Guel, J. C. Aguilar-Márquez, P. R. García-Morán, C. A. Avila-Orta and Z. V. Quiñones-Jurado, *Coatings*, 2024, **14**, 1099.
12 D. Bergé-Lefranc, C. Vagner, O. Schäf, P. Boulet, H. Pizzala, J. L. Paillaud and R. Denoyel, in *Studies in Surface Science and Catalysis*, ed. R. Xu, Z. Gao, J. Chen and W. Yan, Elsevier, 2007, vol. 170, pp. 1015–1020.
13 S. Pourshahrestani, E. Zeimaran, I. Djordjevic, N. A. Kadri and M. R. Towler, *Mater. Sci. Eng., C*, 2016, **58**, 1255–1268.

14 N. Ninan, M. Muthiah, N. A. B.Yahaya, I.-K. Park, A. Elain, T. W. Wong, S. Thomas and Y. Grohens, *Colloids Surf., B*, 2014, **115**, 244–252.
15 C. Bussy, L. Methven and K. Kostarelos, *Adv. Drug Delivery Rev.*, 2013, **65**, 2127–2134.
16 C. Ye, Q.-M. Gong, F.-P. Lu and J. Liang, *Sep. Purif. Technol.*, 2007, **58**, 2–6.
17 S. Malehmir, M. A. Esmaili, M. Khaksary Mahabady, A. Sobhani-Nasab, A. Atapour, M. R. Ganjali, A. Ghasemi and A. Moradi Hasan-Abad, *Front. Chem.*, 2023, **11**, 1249134.
18 S. Li, M. G. Sharaf, L. Zhang, D. S. Wishart, M. Tonelli and L. D. Unsworth, *Macromol. Biosci.*, 2024, **24**, 2300133.
19 H. Kaur, S. S. Chandel, A. Karmakar, S. Sinha-Ray, V. Krishnan and R. R. Koner, *Chem. Eng. J.*, 2022, **443**, 136212.
20 A. Karmakar, S. Hazra and A. J. L. Pombeiro, *Coord. Chem. Rev.*, 2022, **453**, 214314.
21 A. Karmakar, A. A. C. D. Santos, P. Liu, A. V. Gurbanov, J. Pires, E. C. B. A. Alegria, K. I. Hasanov, M. F. C. Guedes da Silva, Z. Wang and A. J. L. Pombeiro, *Inorg. Chem.*, 2024, **63**, 13321–13337.
22 C.-X. Yang, C. Liu, Y.-M. Cao and X.-P. Yan, *RSC Adv.*, 2014, **4**, 40824–40827.
23 K. Dymek, G. Kurowski, Ł. Kuterasiński, R. Jędrzejczyk, M. Szumera, M. Sitarz, A. Pajdak, Ł. Kurach, A. Boguszewska-Czubara and P. J. Jodłowski, *ACS Appl. Mater. Interfaces*, 2021, **13**, 45149–45160.
24 L.-E. Deng, M. Guo, Y. Deng, Y. Pan, X. Wang, G. Maduraiveeran, J. Liu and C. Lu, *Pharmaceutics*, 2024, **16**, 793.
25 T. Yıldız and I. Erucar, *Chem. Eng. J.*, 2022, **431**, 134263.
26 H. Cuchiaro, J. Thai and R. R.Tuttle, Exploring the parameter space of *p*-cresyl sulfate adsorption in metal–organic frameworks, *ACS Appl. Mater. Interfaces*, 2020, **12**(20), 22572–22580, DOI: 10.1021/acsami.0c04203.
27 W. Li, Y. Li, X. Wen, Y. Teng, J. Wang, T. Yang, X. Li, L. Li and C. Wang, *J. Membr. Sci.*, 2022, **648**, 120369.
28 R. M. Abdelhameed, M. Rehan and H. E. Emam, *Carbohydr. Polym.*, 2018, **195**, 460–467.
29 R. Abazari, S. Sanati, M. A. Bajaber, M. S. Javed, P. C. Junk, A. K. Nanjundan, J. Qian and D. P. Dubal, *Small*, 2024, **20**, 2306353.
30 M. Zhang, L. Li, L. Lei, K. Kang and C. Xiao, *ACS Appl. Mater. Interfaces*, 2022, **14**, 55354–55364.
31 T. Islamoglu, K. Otake, P. Li, C. T. Buru, A. W. Peters, I. Akpinar, S. J. Garibay and O. K. Farha, *CrystEngComm*, 2018, **20**, 5913–5918.
32 S. Kato, K. Otake, H. Chen, I. Akpinar, C. T. Buru, T. Islamoglu, R. Q. Snurr and O. K. Farha, *J. Am. Chem. Soc.*, 2019, **141**, 2568–2576.
33 Z. Chao, J. Li, W. Jiang, C. Zhang, J. Ji, X. Hua, L. Xu, L. Han and L. Jia, *Mater. Chem. Front.*, 2021, **5**, 7617–7627.
34 J. H. Cavka, S. Jakobsen, U. Olsbye, N. Guillou, C. Lamberti, S. Bordiga and K. P. Lillerud, *J. Am. Chem. Soc.*, 2008, **130**, 13850–13851.
35 T. C. Wang, N. A. Vermeulen, I. S. Kim, A. B. F. Martinson, J. F. Stoddart, J. T. Hupp and O. K. Farha, *Nat. Protoc.*, 2016, **11**, 149–162.
36 J. E. Mondloch, W. Bury, D. Fairen-Jimenez, S. Kwon, E. J. DeMarco, M. H. Weston, A. A. Sarjeant, S. T. Nguyen, P. C. Stair, R. Q. Snurr, O. K. Farha and J. T. Hupp, *J. Am. Chem. Soc.*, 2013, **135**, 10294–10297.
37 A. R. Heiba, M. O. Abdel-Salam, T. Yoon and E. El Sawy, *Nanoscale*, 2025, **17**, 459–473.
38 Y. Gu, B. A. Anjali, S. Yoon, Y. Choe, Y. G. Chung and D.-W. Park, *J. Mater. Chem. A*, 2022, **10**, 10051–10061.
39 L. Hao, M. J. Hurlock, X. Li, G. Ding, K. W. Kriegsman, X. Guo and Q. Zhang, *Catal. Today*, 2020, **350**, 64–70.
40 P. Li, J. A. Modica, A. J. Howarth, E. Vargas, L. P. Z. Moghadam, R. Q. Snurr, M. Mrksich, J. T. Hupp and O. K. Farha, *Chem*, 2016, **1**, 154–169.
41 F. Gabriel, A. Roussey, S. Sousa Nobre and A. Carella, *J. Mater. Chem. C*, 2024, **12**, 11378–11385.
42 S. Wang, J. Liang, Y. Chen, X. Liu, D. Tong, Y. Li, W. Zhao, B. Su and C. Zhao, *Regen. Biomater.*, 2025, **12**, rbaf082.
43 Y. Liu, X. Peng, Z. Hu, M. Yu, J. Fu and Y. Huang, *Mater. Sci. Eng., C*, 2021, **121**, 111879.
44 A. Paul, K. Das, A. Karmakar, M. F. C. G. da Silva and A. J. L. Pombeiro, *Dalton Trans.*, 2020, **49**, 12970–12984.
45 A. Karmakar, A. Paul, I. R. M. Santos, P. M. R. Santos, E. P. Sabatini, A. V. Gurbanov, M. F. C. Guedes da Silva and A. J. L. Pombeiro, *Cryst. Growth Des.*, 2022, **22**, 2248–2265.
46 H. Strathmann and K. Kock, *Desalination*, 1977, **21**, 241–255.
47 M. C. Andrade, J. C. Pereira, N. de Almeida, P. Marques, M. Faria and M. C. Gonçalves, *Carbohydr. Polym.*, 2021, **261**, 117813.
48 I. Peixoto, M. Faria and M. C. Gonçalves, *Membranes*, 2020, **10**, 195.
49 P. Almeida, R. F. Pires, D. Brilhante, A. Macêdo, V. D. B. Bonifácio and M. Faria, *Sep. Purif. Technol.*, 2025, **359**, 130519.
50 J. M. Carr, D. S. Langhe, M. T. Ponting, A. Hiltner and E. Baer, *J. Mater. Res.*, 2012, **27**, 1326–1350.
51 M. Faria, C. Moreira, T. Eusébio, P. Brogueira and M. N. de Pinho, *Cellulose*, 2020, **27**, 3847–3869.
52 P. Deria, W. Bury, I. Hod, C.-W. Kung, O. Karagiaridi, J. T. Hupp and O. K. Farha, *Inorg. Chem.*, 2015, **54**, 2185–2192.
53 D. Kim and D. Stamatialis, *J. Membr. Sci.*, 2020, **609**, 118187.
54 T. C. Wang, N. A. Vermeulen, I. S. Kim, A. B. F. Martinson, J. F. Stoddart, J. T. Hupp and O. K. Farha, *Nat. Protoc.*, 2016, **11**, 149–162.
55 A. Lui, F. D. F. Talbot, A. Fouda, T. Matsuura and S. Sourirajan, *J. Appl. Polym. Sci.*, 1988, **36**, 1809–1820.
56 J. F. Guerreiro, M. Pereira da Silva, M. Bordonhos, M. Minhalma, M. L. Pinto and M. N. de Pinho, *Desalination*, 2023, **565**, 116860.
57 M. D. Afonso and M. N. De Pinho, *Desalination*, 1990, **79**, 115–124.
58 F. S. C. Rodrigues, S. B. Gonçalves, R. F. Pires, R. Bexiga and M. Faria, *Int. J. Adv. Manuf. Technol.*, 2025, **141**, 5339–5357.
59 F. Norouzi, A. Gharekhani, A. Jouyban and A. Shayanfar, *Chem. Pap.*, 2021, **75**, 3505–3511.

